

Physical Foundations, Models, and Methods of Diffusion Magnetic Resonance Imaging of the Brain: A Review

LUDOVICO MINATI,¹ WŁADYSŁAW P. WĘGLARZ²

¹ *Scientific Direction Unit and Neuroradiology Unit, Istituto Nazionale Neurologico "Carlo Besta," via Celoria, 11, I-20133 Milano MI, Italy*

² *Department of Magnetic Resonance Imaging, "H. Niewodniczanski" Institute of Nuclear Physics, Polish Academy of Sciences, ul. Radzikowskiego 152, 31-342 Kraków, Poland*

ABSTRACT: The foundations and characteristics of models and methods used in diffusion magnetic resonance imaging, with particular reference to in vivo brain imaging, are reviewed.

The first section introduces Fick's laws, propagators, and the relationship between tissue microstructure and the statistical properties of diffusion of water molecules. The second section introduces the diffusion-weighted signal in terms of diffusion of magnetization (Bloch–Torrey equation) and of spin-bearing particles (cumulant expansion). The third section is dedicated to the rank-2 tensor model, the *b*-matrix, and the derivation of indexes of anisotropy and shape. The fourth section introduces diffusion in multiple compartments: Gaussian mixture models, relationship between fiber layout, displacement probability and diffusivity, and effect of the *b*-value. The fifth section is devoted to higher-order generalizations of the tensor model: singular value decompositions (SVD), representation of angular diffusivity patterns and derivation of generalized anisotropy (GA) and scaled entropy (SE), and modeling of non-Gaussian diffusion by means of series expansion of Fick's laws. The sixth section covers spherical harmonic decomposition (SHD) and determination of fiber orientation by means of spherical deconvolution. The seventh section presents the Fourier relationship between signal and displacement probability (Q-space imaging, QSI, or diffusion-spectrum imaging, DSI), and reconstruction of orientation-distribution functions (ODF) by means of the Funk–Radon transform (Q-ball imaging, QBI). © 2007 Wiley Periodicals, Inc. Concepts Magn Reson Part A 30A: 278–307, 2007.

Received 15 February 2007; revised 25 June 2007; accepted 28 June 2007

Correspondence to: L. Minati; E-mail: lminati@istituto-besta.it or W.P. Węglarz; E-mail: wladyslaw.weglarz@ifj.edu.pl

Concepts in Magnetic Resonance Part A, Vol. 30A(5) 278–307 (2007)

Published online in Wiley InterScience (www.interscience.wiley.com). DOI 10.1002/cmr.a.20094

© 2007 Wiley Periodicals, Inc.

KEY WORDS: diffusion physics; diffusion-weighted imaging (DWI); generalised diffusion-tensor imaging (GDTI); spherical harmonic decomposition (SHD) and deconvolution; diffusion spectrum imaging (DSI); Q-ball imaging (QBI)

I. INTRODUCTION

By enabling to obtain sections of gross brain anatomy noninvasively, the introduction of computed tomography and, later, magnetic resonance imaging opened new perspectives for medicine and neuroscience. Although based on very different physical principles, both techniques visualize anatomy by obtaining scalar measurements for each voxel. In order to increase the amount of structural information provided, it is necessary to increase spatial resolution.

As an alternative or as a complement to reducing voxel size, one may endeavor to extract more information beyond a scalar. In particular, analyzing the statistical properties of Brownian motion of water molecules captured by the NMR signal can serve as a probe for the characteristics of biological microstructures orders of magnitude smaller than voxels.

Although chemists and physicists have been probing molecular diffusion by means of NMR since the sixties, the first in vivo diffusion imaging studies date back to the work of Le Bihan and Moseley in the eighties (1–4). Today, diffusion imaging is widely accepted as an important tool in the clinical and research routine, mostly for brain imaging. For example, it provides the earliest and most sensitive marker

of ischemia, it provides quantitative indexes of anatomical connectivity strongly correlating with clinical scores, it enables to reconstruct the path of axonal bundles in three dimensions (5).

These successes were made possible by limited experimental requirements, stemming from two simplifying assumptions, namely presence of a single directional diffusivity maximum and Gaussian nature of the diffusion process. However, the former assumption causes significant measurement bias in areas of the brain in which structures are heterogeneously oriented, and the latter one results in loss of information about hindrance and restriction of diffusion.

Research into models and methods removing these assumptions produced a relatively large body of literature, with formalisms borrowing from several branches of physics. Due to its relative novelty, this field of research has been lacking a review to serve as an easily accessible introduction.

This pedagogically-oriented review is intended to guide the reader through the foundations and characteristics of these advanced models and methods.

The focus is on theory rather than on experimental and computational issues. The reader new to the field of diffusion imaging may in particular benefit from the two-part review by Price, covering basic theory and experimental aspects (6, 7). The present review does not cover in vitro diffusion spectroscopy of porous materials and biological tissues, which has developed along different lines thanks to less restrictive experimental conditions. It also does not cover fiber tractography.

II. SELF DIFFUSION OF WATER MOLECULES IN THE BRAIN PARENCHYMA

Diffusion is the process by which matter is irreversibly transported as a result of random molecular motion. It belongs to the family of irreversible processes like heat conductivity or electric conductivity, the thermodynamics of which is described by general equations relating fluxes (\mathbf{J}_i) and forces ($\mathbf{X} = -\nabla F(\mathbf{r}, t)$), $\mathbf{J}_i = \sum_j L_{ij} \mathbf{X}_j$, where $L_{ij} = L_{ji}$ are coefficients of proportionality (8–11).

The classical phenomenological description of diffusion is based on the assumption of concentration

Abbreviations

ANOVA	analysis of variance
DKI	diffusional kurtosis imaging
DSI	diffusion spectrum imaging
DTI	diffusion tensor imaging
EAP	ensemble average propagator
FA	fractional anisotropy
FMI	fiber multiplicity index
FRT	Funk–Radon transform
GA	generalized anisotropy
GDTI	generalized diffusion tensor imaging
HARDI	high angular resolution diffusion imaging
IVOH	intravoxel orientational heterogeneity
LI	linear index
ODF	orientation density (or distribution) function
PDF	probability density function
PGSE	pulsed-gradient spin-echo
QBI	Q-ball imaging
QSI	Q-space imaging
RA	relative anisotropy
SE	scaled entropy
SGP	short gradient pulse
SHD	spherical harmonic decomposition
SI	spherical index
SVD	singular value decomposition

gradients of molecules of interest; in a homogeneous fluid, such as water, these can be established by introducing tracer molecules (e.g., by using inks or isotopic labeling) of spatial distribution known at the time origin. Even though at the microscopic scale it is not possible to predict which way a particular molecule will move at a given time, at the macroscopic level a definite fraction of molecules will cross a given section in a time interval, resulting in a net transfer if there is a concentration gradient (11).

This is expressed in Fick's first law, which in one dimension can be written as

$$J = -D \frac{\partial C}{\partial x}, \quad [1]$$

where J is the molecular flux density, D is known as diffusion coefficient (usually expressed in $\text{mm}^2 \text{s}^{-1}$), and C is the concentration of molecules (11, 12).

Since mass is conserved, we can write

$$\frac{\partial C}{\partial t} = -\frac{\partial J}{\partial x}. \quad [2]$$

Substitution of Eq. [1] in Eq. [2] gives

$$\frac{\partial C}{\partial t} = D \frac{\partial^2 C}{\partial x^2}, \quad [3]$$

which is known as Fick's second law (11, 12).

For isotropic diffusion in three dimensions, Eq. [1] becomes

$$\mathbf{J} = -D \nabla C, \quad [4]$$

which is equivalent to

$$\begin{pmatrix} J_x \\ J_y \\ J_z \end{pmatrix} = -D \begin{pmatrix} \frac{\partial C}{\partial x} \\ \frac{\partial C}{\partial y} \\ \frac{\partial C}{\partial z} \end{pmatrix}. \quad [5]$$

Equation [2] becomes

$$\frac{\partial C}{\partial t} = -\nabla \cdot \mathbf{J}, \quad [6]$$

which is equivalent to

$$\frac{\partial C}{\partial t} = -\left(\frac{\partial J_x}{\partial x} + \frac{\partial J_y}{\partial y} + \frac{\partial J_z}{\partial z} \right). \quad [7]$$

Combining Eqs. [4] and [6], we obtain Fick's second law in three dimensions

$$\frac{\partial C}{\partial t} = \nabla \cdot (D \nabla C), \quad [8]$$

which, provided D is homogeneous, is equivalent to

$$\frac{\partial C}{\partial t} = D \left(\frac{\partial^2 C}{\partial x^2} + \frac{\partial^2 C}{\partial y^2} + \frac{\partial^2 C}{\partial z^2} \right). \quad [9]$$

Let us consider the case of anisotropic diffusion, for which the concentration vector ∇C and the molecular flux vector \mathbf{J} are not oppositely oriented. It is natural to relate them with a 3×3 matrix:

$$\mathbf{J} = -\mathbf{D} \nabla C, \quad [10]$$

where the \mathbf{D} matrix represents a rank-2 diffusion tensor. While the scalar diffusion coefficient D relates the magnitudes of vectors \mathbf{J} and ∇C , the diffusion tensor \mathbf{D} relates both their magnitudes and orientations.

The diffusion tensor has the form

$$\mathbf{D} = \begin{pmatrix} D_{xx} & D_{xy} & D_{xz} \\ D_{yx} & D_{yy} & D_{yz} \\ D_{zx} & D_{zy} & D_{zz} \end{pmatrix}, \quad [11]$$

and it can be shown that \mathbf{D} is positive definite and symmetric (10, 11, 13).

The diffusion tensor can be thus decomposed

$$\mathbf{D} = \mathbf{R} \mathbf{\Lambda} \mathbf{R}^T, \quad [12]$$

where $\mathbf{R} = (\mathbf{e}_1 \mathbf{e}_2 \mathbf{e}_3)$ is a matrix of the column eigenvectors \mathbf{e}_v and $\mathbf{\Lambda} = \text{diag}(\lambda_1 \lambda_2 \lambda_3)$ is a diagonal matrix of the eigenvalues λ_v . It is usual to sort the eigenvalues and eigenvectors, so that $\lambda_1 \geq \lambda_2 \geq \lambda_3$. Geometrically the diffusion tensor can be represented by a triaxial ellipsoid in the reference frame of the eigenvectors (14).

Thermally-induced Brownian motion takes place regardless of the initial concentration of molecules. For the case of homogeneous initial concentration, the net flux is zero and the process is known as *self-diffusion* (10, 11). Its description is possible in terms of *probability density functions* (PDFs), i.e., in terms of distributions of the probability of finding a given particle at specific position, at given time. More specifically, let us consider the probability for a given molecule at position \mathbf{r} to undergo a displacement to \mathbf{r}' during time interval τ : the corresponding function is known as a *propagator*, and can be written as $P(\mathbf{r}, \mathbf{r}', \tau)$ (11, 15, 16).

Considering \mathbf{J} as a flux of probability density, it is possible to rewrite Fick's first law as

$$\mathbf{J} = -D \nabla P. \quad [13]$$

The continuity theorem gives that

$$\frac{\partial P}{\partial t} = -\nabla \cdot \mathbf{J}, \quad [14]$$

from which we obtain the *Fokker–Planck equation*, corresponding to Fick’s second law:

$$\frac{\partial P}{\partial t} = \nabla \cdot (D\nabla P). \quad [15]$$

This equation is used as a starting point for the solution of problems related to stochastic processes, irreversibility, and spin relaxation. Although it was introduced here by correspondence with the classical Fick’s equation, it can be derived directly from the elementary model of random walk (8, 17).

In this review, we are concerned with the macroscopic properties of a process which arises from the motion of very large numbers of particles. The average over a number of particles is known as *ensemble average*, and is usually written as $\langle f(x) \rangle$; it is given by

$$\langle f(x) \rangle = \int f(x)p(x)dx, \quad [16]$$

where $p(x)$ is the distribution of x . The ensemble average propagator (EAP), or *displacement PDF*, can be written as

$$P(\mathbf{R}, \tau) = \int P(\mathbf{r}, \mathbf{r}', \tau)\rho(\mathbf{r})d\mathbf{r}, \quad [17]$$

where $\mathbf{R} = \mathbf{r} - \mathbf{r}'$, and where $\rho(\mathbf{r})$ is the initial density of molecules (15, 16).

For the simplest case, free diffusion in one dimension, the EAP is Gaussian,

$$P(X, \tau) = \frac{1}{\sqrt{(2\pi\sigma^2)}} \exp\left(-\frac{X^2}{2\sigma^2}\right), \quad [18]$$

where X is the one-dimensional displacement (11, 15, 16).

Given that the process is a random walk, the variance σ^2 is the sum of the variances of the elementary steps; since they are equal, it is proportional to total time

$$\sigma^2 = 2D\tau. \quad [19]$$

The standard deviation defines the *characteristic diffusion length*

$$\ell = \sqrt{2D\tau}, \quad [20]$$

which is also referred to as *Einstein length*, or root-mean-square displacement; in three dimensions it becomes (11, 18)

$$\ell = \sqrt{6D\tau}. \quad [21]$$

Equation [18] can be written for three dimensions as

$$P(\mathbf{R}, \tau) = \frac{1}{\sqrt{(4D\pi\tau)^3}} \exp\left(-\frac{|\mathbf{R}|^2}{4D\tau}\right), \quad [22]$$

from which extension to anisotropic diffusion is not difficult (11, 15, 16)

$$P(\mathbf{R}, \tau) = \frac{1}{\sqrt{|\mathbf{D}|(4\pi\tau)^3}} \exp\left(-\frac{\mathbf{R}^T \mathbf{D}^{-1} \mathbf{R}}{4\tau}\right). \quad [23]$$

Although anisotropic and to a good approximation Gaussian diffusion does occur in liquid crystals, in the brain parenchyma anisotropic Gaussian diffusion embodies a contradiction: where can anisotropy arise from, if not from the presence of barriers, which render diffusion non-Gaussian? In this context it is unphysical in nature, and is to be considered only as an approximation of the actual diffusion propagator.

When diffusion takes place in presence of barriers, the diffusion propagator may take a very complex form, and is not only a function of relative displacement, but of absolute position as well; it is the ensemble averaging which enables us to consider $P(\mathbf{R}, \tau)$. Provided that there is no net flux of molecules ($\mathbf{J} = 0$), one has $\int_{-\infty}^0 P(X, \tau)dX = \int_0^{\infty} P(X, \tau)dX$; since diffusion is a radially symmetric process, one has $P(\mathbf{R}, \tau) = P(-\mathbf{R}, \tau)$.

Diffusion of water molecules in the brain parenchyma takes place in multiple intracellular and extracellular compartments. In the simplified case of impermeable cell membranes, intracellular diffusion is restricted within boundaries in space (i.e., it takes place in disconnected pores), while extracellular diffusion is hindered by collisions with barriers (i.e., it takes place in connected spaces). The volume proportions of the intracellular and extracellular compartments are about 80% and 20% respectively (19, 20).

Diffusivity as measured from the motion of molecules in a brain voxel of finite volume in a finite time interval is determined not only by the properties of the diffusing medium, by the geometry, and permeability of barriers, but also by measurement conditions such as the diffusion time τ : in recognition of this fact, it is often referred to as *apparent diffusivity* D_{app} , or as *apparent diffusion coefficient*. The same applies to the apparent diffusion tensor \mathbf{D}_{app} . In liter-

ature, D_{app} and \mathbf{D}_{app} are sometimes written as D and \mathbf{D} for brevity; this is also the case for the next sections of this review.

For the case of free diffusion, we have $D_{\text{app}} = D_0$, where D_0 is the intrinsic diffusivity of the medium, which depends on temperature T and viscosity η with (11)

$$D_0 \propto \frac{T}{\eta}. \quad [24]$$

The intrinsic diffusivity D_0 in the intracellular compartment is lower than that in the extracellular one because of higher viscosity.

It is instructive to explore the relationship between τ and D_{app} through some limiting cases.

For short τ , barriers have a negligible influence, because the fraction of molecules striking the barriers is small, hence

$$\lim_{\tau \rightarrow 0} D_{\text{app}}(\tau) = D_0; \quad [25]$$

in this limit diffusion is isotropic (16).

In the opposite extreme, $\tau \rightarrow \infty$, hindered and restricted diffusion have different properties.

In the long-time limit ($\tau \gg a^2/D_0$ for a spherical pore of diameter a), known as the *Markovian regime*, molecules lose memory of their initial position \mathbf{r} and of the diffusional process. For the case of diffusion restricted in an isolated pore with impermeable and reflecting boundaries, the propagator assumes the shape of the pore

$$P(\mathbf{r}, \mathbf{r}', \tau \rightarrow \infty) = \chi(\mathbf{r}'), \quad [26]$$

where $\chi(\mathbf{r}')$ is the *pore shape function*, which is homogeneous within pore boundaries, zero outside, and for which $\int \chi(\mathbf{r}) d\mathbf{r} = 1$; as explained in the seventh section, the EAP becomes the autocorrelation function of $\chi(\mathbf{r})$ (6, 16, 21).

Since the maximum displacement ℓ_{max} is set by the pore boundaries,

$$\lim_{\tau \rightarrow \infty} \ell(\tau) \leq \ell_{\text{max}}; \quad [27]$$

from Eq. [20] we have

$$\lim_{\tau \rightarrow \infty} D_{\text{app}}(\tau) = 0. \quad [28]$$

For hindered diffusion the situation is more complex; it is found experimentally that

$$\lim_{\tau \rightarrow \infty} D_{\text{app}}(\tau) = D_{\text{long}}, \quad [29]$$

where the coefficient $\sqrt{D_0/D_{\text{app}}} \geq 1$ is known as *tortuosity* (18, 21).

These simplified long-time limits do not apply in biological systems for a number of reasons. First, pores are rarely isolated, and diffusion occurs in highly connected spaces. Second, they do not account for the fact that biological membranes are permeable, and that therefore there is exchange of water molecules between intracellular and extracellular compartments. A more detailed discussion of the effects of membrane permeability can be found in Refs. (19, 20, 22). Third, water molecules may be actively pumped through membranes as a result of physiological activity and bulk flow of extracellular fluid occurs due to cardiac pulsatility. Fourth, interaction between membranes and water molecules causes loss of transverse magnetization due to dephasing, leading to an apparent absorption effect (19, 20).

The brain parenchyma is composed of neural and glial cells, the latter outnumbering the former by a factor of about 10. In grey matter, the bodies of neural cells and dendrites are not microstructurally arranged in a directional manner, resulting in relatively isotropic and homogeneous water diffusion. In white matter, bundles of axons, long tube-shaped extensions of the body of neural cells whose purpose is to conduct electric pulses, have a clear directional orientation. Glial cells of heterogeneous shape and size are found in both grey and white matter (23).

As represented in Fig. 1, axons contain microtubules and neurofilaments, two intracellular structures that run along the axon. In some areas axons are myelinated, i.e., have their cell membrane covered by a fatty substance, known as myelin, whose purpose is to control the axon's electrical impedance by its dielectric properties, in remarkable similarity to coaxial cables. The permeability of myelin sheaths

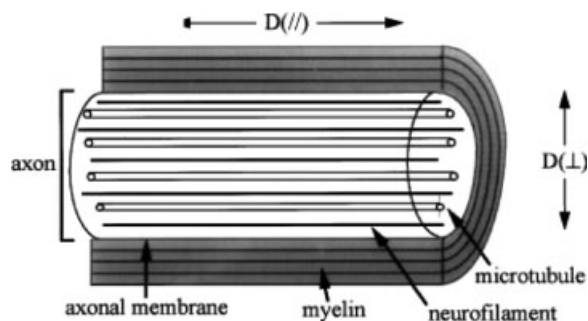


Figure 1 Directionally oriented structures in axons. (Reproduced from (23) with permission from John Wiley & Sons.) Diffusion is highly anisotropic. Putative determinants of anisotropy include intracellular microtubules and neurofilaments, the axonal membrane, and the extracellular myelin sheath.

for water molecules is very low; myelin is arranged in concentric layers, separated by spaces in which water molecules can diffuse (23).

Depending on the location and degree of maturation in the healthy human brain the axonal diameter varies from about 4 to about 10 μm , the thickness of the myelin sheath ranges from 500 nm to about 2 μm , and the extraaxonal separation varies from about 500 nm to about 2 μm (23).

Diffusion within axonal bundles is highly anisotropic: longitudinal diffusivity D_{\parallel} is 2–5 times larger than transverse diffusivity D_{\perp} . The exact microstructural features which underlie the measured anisotropy remained matter of debate until recently. Postulated sources of anisotropy include both intracellular and extracellular structures: axonal membranes, myelin sheaths, microtubules, and fast axonal transport (a physiological mechanism of intracellular transport of molecules) (23, 24).

One of the first studies involved measurements on the naturally nonmyelinated olfactory nerve of the garfish and on the walking leg nerve of the lobster. As reported by Beaulieu and Allen, the anisotropy ratio (defined as D_{\parallel}/D_{\perp}) was found to be similar to that of myelinated fibers in the same species. Other groups later studied the spinal cord of rats genetically engineered in order not to have myelination, and found that the anisotropy ratio was about 4.5 in control and 3.5 in mutated rats (23, 24). Beaulieu and Allen evaluated the contribution of microtubules and fast axonal transport by comparing excised nerves stored in a neutral buffer solution with nerves stored in a buffer containing vinblastine, a compound which is known to destroy microtubules and to inhibit fast axonal transport. No significant differences in anisotropy were reported, suggesting that the contributions of intracellular transport and microtubules are negligible. Potential contributions from magnetic susceptibility differences were evaluated, and found to be negligible as well (23, 24). One therefore concludes that diffusional anisotropy in white matter is primarily determined by axonal membranes, with an additional contribution (on the order of 30%) from myelin sheaths.

III. DIFFUSION-WEIGHTED SIGNAL: BLOCH–TORREY EQUATION AND CUMULANT EXPANSION

In 1956 Torrey proposed the addition of two terms to the Bloch equation to account for flow and diffusion of magnetization

$$\frac{\partial \mathbf{M}}{\partial t} = \gamma \mathbf{M} \times \mathbf{B} + \begin{pmatrix} -\frac{1}{T_2} & 0 & 0 \\ 0 & -\frac{1}{T_2} & 0 \\ 0 & 0 & -\frac{1}{T_1} \end{pmatrix} \mathbf{M} + \begin{pmatrix} 0 \\ 0 \\ \frac{M_0}{T_1} \end{pmatrix} - \nabla \cdot \mathbf{v} \mathbf{M} + \nabla \cdot \mathbf{D} \nabla \mathbf{M}, \quad [30]$$

where \mathbf{M} represents the magnetization vector, \mathbf{B} the static magnetic field vector, T_1 the longitudinal (spin–lattice) relaxation time, T_2 the transverse (spin–spin) relaxation time, M_0 the thermal equilibrium magnetization, and where \mathbf{v} is the flow velocity, and \mathbf{D} the rank-2 diffusion tensor. The effect of the diffusion term is to introduce signal attenuation; the effect of the flow term is to introduce a net phase shift. This is known as the *Bloch–Torrey* equation (25). In the remainder of this section, we shall limit ourselves to the case of absence of flow.

About a decade later, Stejskal and Tanner introduced the *pulsed-gradient spin-echo* (PGSE) sequence, in which two identical gradient pulses are inserted on both sides of the π refocusing pulse of a conventional spin-echo sequence (1, 2).

As represented in Fig. 2, for simplicity and without loss of generality, we shall assume that the diffusion-weighting gradients are rectangular, even though in practice this condition cannot be realized due to slew-rate limitations; we shall also take the time origin to correspond to the time the first gradient pulse is switched on. The gradient intensity is referred to as g , the duration as δ , and the spacing as Δ (which corresponds to the diffusion time τ).

While diffusion-weighting gradients can be applied along any direction, for the sake of simplicity and without loss of generality, let us consider the x -axis, and a spin at position x during the first gradient pulse and at position x' during the second gradient pulse.

Owing to the linear relationship between precession rate and the applied magnetic field, the first pulse induces dephasing

$$\phi_1 = \gamma \int_0^{\delta} g x \, dt = \gamma g \delta x, \quad [31]$$

while the second pulse induces dephasing

$$\phi_2 = \gamma \int_{\Delta}^{\Delta+\delta} g x' \, dt = \gamma g \delta x', \quad [32]$$

where γ is the gyromagnetic ratio in $\text{rad s}^{-1} \text{T}^{-1}$.

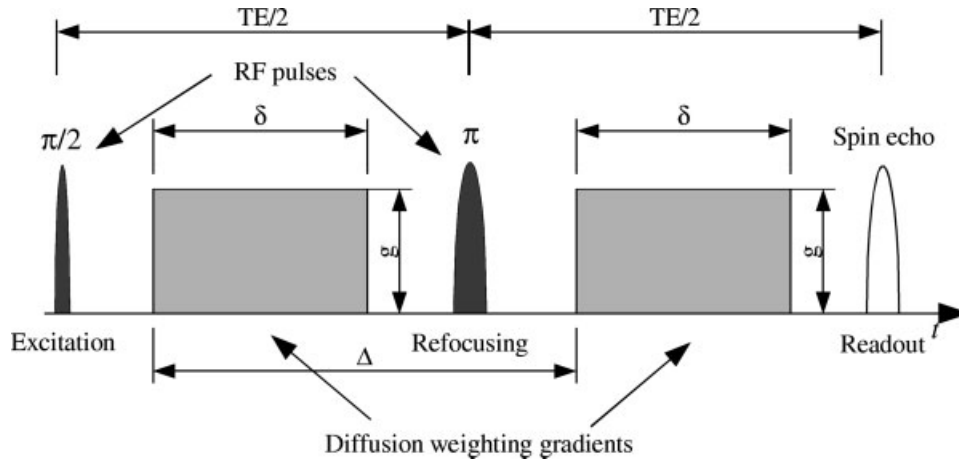


Figure 2 The PGSE (or, for historical reasons, Stejskal–Tanner) sequence. For the idealised case of rectangular gradient pulses, g represents gradient intensity, gradient duration, and δ gradient spacing, that is, diffusion time (corresponding to the diffusion time τ).

Since the sign of ϕ_1 is inverted by the π pulse, we obtain

$$\phi = \phi_2 - \phi_1 = \gamma g \delta (x' - x); \quad [33]$$

this is a simple linear relationship between displacement $x' - x$ and net dephasing ϕ , which is null for static spins ($I, 2$).

It is of central importance to realize that due to the random nature of displacement $x' - x$ the dephasing ϕ is a random variable; as a consequence, after ensemble averaging the result is signal attenuation, and not a net phase shift.

These equations embed an important assumption, namely that x and x' remain constant while the gradient is on; this corresponds to assuming δ is infinitesimally short, and is therefore known as the *short gradient pulse* (SGP) condition. The formula for net dephasing becomes more complex if this assumption is removed (26). Experimentally the effect of violating this assumption may be reduced by ensuring $\delta = l^2/2D$, where l represents pore diameter; however, this is often not possible under in vivo conditions due to slew-rate limitations. The effect of finite δ is underestimation of σ (from Eq. [19]), that is, of diffusivity: Assaf et al. determined in vivo that sweeping δ from 4.5 to 72 ms reduced σ by a factor of about two, which corresponds to about 30% for diffusivity (27, 28).

Diffusion-weighted signal can be modeled in terms of diffusion of magnetization, or in terms of diffusion of spin-bearing particles. The former approach involves solving the Bloch–Torrey equation, the latter is based on cumulant expansion. We

shall review both of them, showing that they are equivalent for the case of Gaussian diffusion.

Let us start considering diffusion of magnetization.

Since in a PGSE sequence a time-dependent diffusion-weighting gradient $\mathbf{g}(t)$ (represented by a column vector) is applied, spins are subject to a magnetic field

$$\mathbf{B}(\mathbf{r}, t) = (0, 0, B_0 + \mathbf{g}(t) \cdot \mathbf{r}), \quad [34]$$

where \mathbf{r} is the spin displacement vector.

Substituting in Eq. [30], and considering complex magnetization m on the transverse plane, we obtain ($I, 2$)

$$\frac{\partial m}{\partial t} = -i\gamma B_0 m - \frac{m}{T_2} - i\gamma \mathbf{r} \cdot \mathbf{g}(t) m + \nabla \cdot (\mathbf{D} \nabla m). \quad [35]$$

In order to eliminate the precession and spin–spin relaxation terms, we can substitute

$$m(\mathbf{r}, t) = \psi(\mathbf{r}, t) \exp\left(-\left(i\gamma B_0 + \frac{1}{T_2}\right)t\right), \quad [36]$$

from which ($I, 2$)

$$\frac{\partial \psi}{\partial t} = -i\gamma \mathbf{r} \cdot \mathbf{g}(t) \psi + \nabla \cdot (\mathbf{D} \nabla \psi). \quad [37]$$

We can further simplify this equation by separating $\psi(\mathbf{r}, t)$ into an imaginary part, which represents the solution without diffusion, and a real part, which represents the attenuation due to diffusion. Given

$$\psi(\mathbf{r}, t) = M(t) \exp(-i\mathbf{r} \cdot \mathbf{G}(t)), \quad [38]$$

where

$$\mathbf{G}(t) = \gamma \int_0^t \mathbf{g}(t') dt', \quad [39]$$

and where the sign of $\mathbf{g}(t')$ is inverted for all gradient pulses following the π -pulse, we obtain

$$\frac{dM}{dt} = M(t) \nabla \cdot (\mathbf{D} \nabla \exp(-i\mathbf{r} \cdot \mathbf{G}(t))), \quad [40]$$

from which (1, 2)

$$\frac{dM}{dt} = -M(t) \mathbf{G}(t)^T \mathbf{D} \mathbf{G}(t). \quad [41]$$

This equation is solved by

$$M(t) = M(0) \exp\left(-\int_0^t \mathbf{G}(t')^T \mathbf{D} \mathbf{G}(t') dt'\right). \quad [42]$$

It is convenient to introduce a quantity characterizing the “strength” of diffusion-weighting

$$b = \int_0^{\text{TE}} \mathbf{G}(t')^T \mathbf{G}(t') dt', \quad [43]$$

where TE is the echo time of the PGSE sequence; this quantity is known as the *b-value* or *b-factor*, and has units of s mm^{-2} (29).

Equation [42] can be rewritten as

$$s = \exp(-\mathbf{b} \mathbf{u}^T \mathbf{D} \mathbf{u}), \quad [44]$$

where \mathbf{u} is the unit vector corresponding to the direction of the diffusion-sensitizing gradient, and the normalized signal $s = M(\text{TE})/M(0)$. This equation is known as the *Stejskal–Tanner* equation. In in vivo experiments the phase of M is discarded in order to remove physiological contamination; this corresponds to assuming the flow term in Eq. [30] is null. For isotropic diffusion, Eq. [44] takes the simpler form

$$s = \exp(-bD). \quad [45]$$

For a PGSE sequence, from Eq. [43] we obtain

$$b = \gamma^2 \int_0^\delta \left(\int_0^t g dt'\right)^2 dt + \gamma^2 \int_\delta^\Delta \left(\int_\delta^t g dt'\right)^2 dt + \gamma^2 \int_\Delta^{\Delta+\delta} \left(\int_0^\delta g dt' - \int_\Delta^t g dt'\right)^2 dt, \quad [46]$$

from which

$$b = \gamma^2 \delta^2 g^2 \left(\Delta - \frac{\delta}{3}\right). \quad [47]$$

It is important to note that in this derivation the SGP condition has not been used; the $-\delta/3$ term in Eq. [47] accounts for diffusion occurring while the gradient is on. Equation 43 is also valid for other gradient pulse types (30).

Let us now turn to diffusion of spin-bearing particles. For simplicity, we shall assume that diffusion is isotropic.

Assuming δ is infinitesimally short (SGP condition), complex signal from one precessing spin can be written as

$$c = \exp(i\phi) = \exp(i\gamma g \delta X), \quad [48]$$

where ϕ is the net dephasing and X is the displacement along the gradient direction.

Since the signal from a voxel is the ensemble average of signal from individual spins with displacement X as the random variable, we can write

$$c = \langle \exp(i\gamma g \delta X) \rangle = \int_{-\infty}^{\infty} \exp(i\gamma g \delta X) P(X, \tau) dX, \quad [49]$$

where in this case c represents complex normalized signal.

We recognize that, thanks to the presence of the exponential term, this has the familiar form of the characteristic function (i.e., of the Fourier transform) of the one-dimensional propagator $P(X, \tau)$. Since the cumulant generating function exists for any distribution, the logarithm of such a function can be thus expanded

$$\ln(c) = \sum_{n=1}^{\infty} k_n \frac{(i\gamma g \delta)^n}{n!}, \quad [50]$$

where k_n are the *cumulants* of the displacement PDF; this is known as cumulant generating function (31). We note that this expansion has the form of a Taylor series in powers of $i\gamma g \delta$.

The first cumulant k_1 is the mean, which, like all other odd-order terms, is zero if the net flux is zero; this is equivalent to assuming $P(X, \tau)$ is even with respect to X . The second cumulant k_2 is the variance. The k_1 and k_2 therefore correspond to the first and second moments, μ_1 and μ_2 . Rearranging Eq. [19], we have

$$\begin{aligned} k_1 &= 0 \\ k_2 &= 2D\Delta. \end{aligned} \quad [51]$$

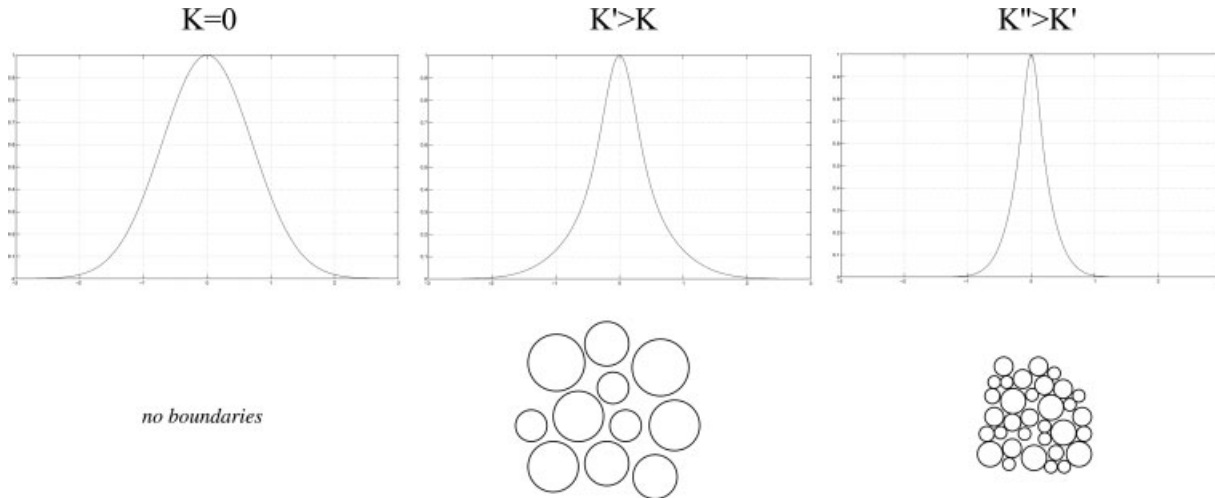


Figure 3 Microstructure, peakedness and kurtosis. For the case of free diffusion, the displacement PDF is Gaussian, so kurtosis is zero, and the width of the displacement PDF is determined uniquely by intrinsic diffusivity. As the density of barriers is increased, the displacement PDF becomes narrower, that is apparent diffusivity decreases, and small displacements become relatively more probable, increasing kurtosis. (Reproduced from (36) with permission from the European Society for Magnetic Resonance in Medicine and Biology.)

Terminating the expansion at the second term, we obtain

$$\ln(s) = -\frac{\gamma^2 g^2 \delta^2}{2} k_2 = -\gamma^2 g^2 \delta^2 \Delta D \approx -bD; \quad [52]$$

for free diffusion, all cumulants except k_2 are zero (32, 33).

Here the $-\delta/3$ term is missing, because in Eq. [48] the SGP condition has been used; cumulant expansion without this assumption is possible, considering $P(X, \tau)$ as the *centre-of-mass propagator*, but considerably more complex (34).

Cumulant expansion offers a natural means to model deviation from Gaussian behavior, introducing higher cumulants

$$\ln(s) = -\frac{\gamma^2 g^2 \delta^2}{2} k_2 + \frac{\gamma^4 g^4 \delta^4}{4!} k_4 - \frac{\gamma^6 g^6 \delta^6}{6!} k_6 + \dots \quad [53]$$

This expansion is useful at low and intermediate b -values, at which deviation from the exponential model becomes appreciable, but has a finite radius of convergence determined by the zeros, and diverges for large b -values (33).

To a first approximation, the effect of the presence of barriers in biological tissues is to render short displacements relatively more probable than long ones with respect to Gaussian diffusion (35). As depicted

in Fig. 3, this corresponds to increasing the “peakedness” of the displacement PDF, which can be quantified by computing the *excess kurtosis*, defined as

$$K = \frac{k_4}{k_2^2}, \quad [54]$$

for Gaussian diffusion $K = 0$. In terms of the moments, excess kurtosis is defined as $K = \mu_4/\mu_2^2 - 3$ (37).

Substituting k_2 from Eq. [51] and rearranging, we obtain

$$k_4 = Kk_2^2 = 4KD^2\Delta^2; \quad [55]$$

from which (35)

$$\ln(s) = -bD + \frac{1}{6}b^2D^2K. \quad [56]$$

Therefore, direct estimation of diffusional kurtosis is possible by means of the cumulant expansion, without resorting to reconstruction of the full displacement PDF using QSI or diffusion spectrum imaging (DSI), introduced in the seventh section; this is sometimes referred to as *diffusional kurtosis imaging* (DKI) (35).

In biological tissues, the PDF is generally leptokurtic, that is $K > 0$, and platokurtosis, that is $K < 0$, is not expected.

The parallel of Eq. [25] for kurtosis is

$$\lim_{\Delta \rightarrow 0} K(\Delta) = 0. \quad [57]$$

In presence of barriers, one expects K to increase with diffusion time; the relationship remains to be elucidated both analytically and experimentally. In biological tissues, leptokurtosis may be induced by membrane reflectivity, reducing net displacement with respect to free diffusion, and by membrane relaxivity, reducing the relative contribution of molecules undergoing long displacements, and may be attenuated by membrane permeability. Platokurtosis is not expected as there is no arrangement of barriers which can render long displacements relatively more probably than the short ones with respect to free diffusion. As a consequence of the layout of barriers, in axonal bundles $K_{\perp} > K_{\parallel}$ (38).

For restricted diffusion, as a consequence of Eq. [27], we have

$$\lim_{\Delta \rightarrow \infty} \phi(\Delta) \leq \phi_{\max}, \quad [58]$$

where ϕ represents net dephasing (from Eq. [33]), from which we can write

$$\lim_{\Delta \rightarrow \infty} s(\Delta) = s_{\min}. \quad [59]$$

This simplified limit does not hold in biological tissues due to the permeability and relaxivity of membranes. Although Le Bihan et al. reported that sweeping Δ from 16 to 79 ms had no significant effect on apparent diffusivity, later studies employing a biexponential model (introduced in the fourth section) found that sweeping Δ in a comparable range affected the measured slow-diffusing component by a factor of about two (39, 40).

Nowadays, in vivo diffusion imaging most commonly relies on a twice-refocused variant of the PGSE sequence, which enables to null the effects of exponentially-decaying eddy currents; although conceptually akin to the PGSE sequence, for this sequence Δ is not well-defined (41).

In NMR diffusion measurements, if one assumes monoexponential signal decay there is an “optimal” b -value between the extremes of zero attenuation and zero signal minimizing the uncertainty in measurement of D_{app} ; an accepted rule-of-thumb is to set $b = 1.1/D$, which for the brain translates to $b \approx 1400 \text{ s mm}^{-2}$ (42). As shown in the fourth section, this empirical rule is invalid when multiple compartments are considered, in which case stronger diffusion-

weighting is necessary to resolve the relative contribution of each compartment.

It is instructive to consider that water self-diffusion is a good probe of tissue microstructure because, for the distribution of compartment sizes found in biological tissues and for the value of $D_0 \approx 1 \times 10^{-3} \text{ mm}^2 \text{ s}^{-1}$, $\ell^2/2D_0 \approx T_2$; the situation would not have been so favorable had D_0 been lower or ℓ larger, as longer diffusion times Δ would have resulted in excessive loss of signal due to spin-spin relaxation.

IV. DIFFUSION-TENSOR IMAGING WITH THE RANK-2 TENSOR MODEL

Equation [44] establishes a relationship between the diffusion-weighted signal s and the diffusion tensor \mathbf{D} , but leaves the problem of how \mathbf{D} can be measured in an MRI experiment. The solution put forward by Stejskal in 1965 is not applicable in its original form, because it is for the laboratory frame of reference, and in an MRI experiment the reference frame of the diffusion tensor in each voxel is not known a priori, and the sample cannot be reoriented in the magnet (2). In 1994 Basser, Mattiello, and Le Bihan showed that \mathbf{D} can be determined solving a linear system of the form

$$\begin{pmatrix} x_1^2 & y_1^2 & z_1^2 & 2x_1y_1 & 2y_1z_1 & 2z_1x_1 \\ \vdots & \vdots & \vdots & \vdots & \vdots & \vdots \\ x_i^2 & y_i^2 & z_i^2 & 2x_iy_i & 2y_iz_i & 2z_ix_i \\ \vdots & \vdots & \vdots & \vdots & \vdots & \vdots \\ x_N^2 & y_N^2 & z_N^2 & 2x_Ny_N & 2y_Nz_N & 2z_Nx_N \end{pmatrix} \begin{pmatrix} D_{xx} \\ D_{yy} \\ D_{zz} \\ D_{xy} \\ D_{yz} \\ D_{zx} \end{pmatrix} = \begin{pmatrix} -\frac{1}{b} \ln(s_1) \\ \vdots \\ -\frac{1}{b} \ln(s_i) \\ \vdots \\ -\frac{1}{b} \ln(s_N) \end{pmatrix}, \quad [60]$$

where N is the number of measurements, $i = 1, \dots, N$, s_i represents normalised signal magnitude for each measurement, and $\mathbf{u}_i = (x_i, y_i, z_i)$ are unit vectors corresponding to the directions of the diffusion-sensitising gradients (43).

In virtue of the fact that it is symmetric, the diffusion tensor has six independent elements; therefore, in principle it could be determined from six diffusion-weighted measurements performed at a b -factor b with noncollinear directions, and one done at $b' \neq$

b. However, in practice a larger number of directions, on the order of 12–30, is necessary in order to obtain reasonably homogeneous uncertainty; the resulting linear system can be solved by the least squares method (42).

The vertices of platonic solids (octahedron, icosahedron, dodecahedron) are frequently chosen as a basis for \mathbf{g}_i , and tessellation (i.e., dividing a surface into elements that have no overlaps and no gaps) may be used to increase the number of vertices. However, the best accuracy is obtained when the sampling vectors are equally spaced on the unit sphere; a physical analogy, proposed by Jones, turns out to be useful: if each direction is made to correspond to a unit charged particle constrained on the surface of a sphere, directions can be optimized in order to minimize the sum of repulsive forces between every possible pair of particles (42).

In MRI sequences, imaging and spoiling gradients introduce additional diffusion-weighting; as they are applied along multiple directions, their effect cannot be represented by a vector. It turns out to be useful to introduce a more general entity, the \mathbf{b} -matrix

$$\mathbf{b} = \begin{pmatrix} b_{xx} & b_{xy} & b_{xz} \\ b_{yx} & b_{yy} & b_{yz} \\ b_{zx} & b_{zy} & b_{zz} \end{pmatrix}. \quad [61]$$

In this matrix, which represents a symmetric rank-2 tensor, the diagonal elements subsume interactions between diffusion-weighting and imaging gradients in the same direction, and off-diagonal elements subsume interactions in orthogonal directions (30, 43).

Introducing the scalar product for rank-2 tensors as

$$\mathbf{A} : \mathbf{B} = \sum_{i=1}^3 \sum_{j=1}^3 A_{ij} B_{ij}, \quad [62]$$

we can write

$$\ln(s) = -\mathbf{b} : \mathbf{D}, \quad [63]$$

from which

$$\ln(s) = -[b_{xx}D_{xx} + b_{yy}D_{yy} + b_{zz}D_{zz} + 2b_{xy}D_{xy} + 2b_{xz}D_{xz} + 2b_{yz}D_{yz}]. \quad [64]$$

The matrix version of Eq. [43] is

$$\mathbf{b} = \int_0^{TE} \mathbf{F}(t') \mathbf{F}(t')^T dt', \quad [65]$$

with

$$\mathbf{F}(t) = \gamma \int_0^t \mathbf{f}(t') dt', \quad [66]$$

where $\mathbf{f}(t)$ represents all gradient pulses including imaging and spoiling gradients, the sign being inverted for all gradient pulses following the π -pulse (39).

Analytical expressions for the \mathbf{b} -matrix can be derived for a given pulse sequence: a method of derivation can be found in (30). Notwithstanding the resulting limitation on accuracy, the effect of imaging and spoiling gradients is often neglected because their strength is typically small compared to that of the diffusion-weighting gradients, simplifying calculations by enabling to use the scalar b -factor $b = b_{xx} + b_{yy} + b_{zz}$ (44). A geometrical method for computing the b -value and an analogy for the effect of cross terms can be found in Ref. (44).

The diffusion tensor measured in the laboratory frame of reference normally has nonzero off-diagonal elements, and may include negative terms; while negative diffusivities are per se unphysical, negative terms may occur as a consequence of the fact that the frame of reference of the tensor is rotated with respect to that of the laboratory. Rotation to the frame of reference of the tensor, in which all off-diagonal terms are zero and all diagonal terms are non-negative (negative eigenvalues are uniquely an effect of measurement error), is accomplished by means of diagonalization (Eq. [12]), which may be performed with the Jacobi iterative method, or with analytical methods (45). A frequently used alternative is the singular value decomposition (SVD), which has the form

$$\mathbf{D} = \sum_{i=1}^3 \sigma_{ii} \mathbf{u}_i \circ \mathbf{v}_i, \quad [67]$$

where \circ is the *outer product*, defined as $\mathbf{u} \circ \mathbf{v} = \mathbf{u} \mathbf{v}^T$, and where \mathbf{u}_i and \mathbf{v}_i are, respectively, the columns of the 3×3 matrices \mathbf{U} and \mathbf{V} . Since \mathbf{D} is positive definite and Hermitian, the elements of the diagonal matrix $\boldsymbol{\sigma}$ correspond to the eigenvalues λ_i and \mathbf{u}_i correspond to the eigenvectors \mathbf{e}_i . An introduction to the SVD can be found in Ref. (46).

Having sorted the eigenvalues so that $\lambda_1 \geq \lambda_2 \geq \lambda_3$, the diffusion tensor can be represented by the ellipsoid

$$\frac{x'^2}{2\lambda_1\tau} + \frac{y'^2}{2\lambda_2\tau} + \frac{z'^2}{2\lambda_3\tau} = 1 \quad [68]$$

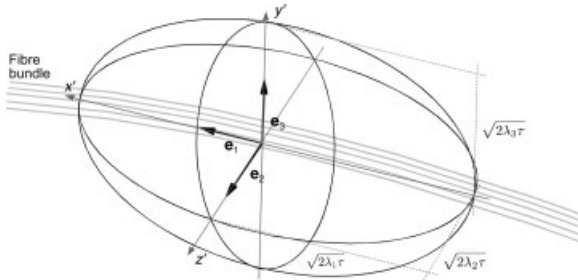


Figure 4 Tangency of the principal eigenvector. Provided that the orientation of axons is coherent, the principal eigenvector (that is, the direction of maximum diffusivity) is tangent to the path of the fibre bundle. The surface of the ellipsoid in this figure corresponds to characteristic length.

in the reference frame of the eigenvectors $\mathbf{e}_1, \mathbf{e}_2, \mathbf{e}_3$, corresponding to x', y', z' (the axes in the reference frame of the tensor) (14). The surface of this ellipsoid corresponds to the characteristic length (see Eq. [20]) for a given diffusion time. It is especially important to note that the surface corresponding to diffusivity will generally not enclose an ellipsoid, but a peanut-shaped volume; this is a consequence of the nonlinear relationship between characteristic length and diffusivity (Eq. [20]).

As a consequence of the fact that for diffusion within an axonal bundle $D_{\parallel} > D_{\perp}$, one can write

$$\frac{d\mathbf{r}(s)}{ds} = \mathbf{e}_1(\mathbf{r}(s)), \quad [69]$$

where $\mathbf{r}(s)$ corresponds to the path of the axonal bundle in space parameterized by the arc length s ; as depicted in Fig. 4, the direction of the principal eigenvector in each voxel is tangent to the path of the bundle (47).

It is desirable to extract from the diffusion tensor field scalar indexes representative of tissue microstructure, and invariant to the rotation of the sample in the scanner. The tensor eigenvalues provide a natural basis.

The average of the eigenvalues, corresponding to the directionally-averaged diffusivity, can be written as

$$\langle D \rangle = \frac{\text{Trace}(\mathbf{D})}{3} = \frac{D_{xx} + D_{yy} + D_{zz}}{3} = \frac{\lambda_1 + \lambda_2 + \lambda_3}{3} = \langle \lambda \rangle, \quad [70]$$

where \mathbf{D} is the diffusion tensor measured in the laboratory reference frame. Since the intrinsic diffusivity of water in the intracellular environment (D_i , see the next section) is lower than that in the extracellular environment (D_e), the apparent diffusivity (D_{app} , frequently shortened to D as above and as discussed in the first section) is often interpreted as an inverse indicator of cellular density (14, 48).

It is useful to decompose the diagonalized diffusion tensor into the sum of an isotropic tensor Λ_{μ} and a traceless deviatoric tensor Λ_{σ}

$$\Lambda = \Lambda_{\mu} + \Lambda_{\sigma} = \langle \lambda \rangle \mathbf{I} + (\Lambda - \langle \lambda \rangle \mathbf{I}), \quad [71]$$

where \mathbf{I} is the identity matrix; as depicted in Fig. 5, Λ_{σ} represents the deviation from isotropic diffusion (14, 48).

Scalar measures of diffusional anisotropy can be obtained in a natural way by comparing the magnitude of the isotropic tensor Λ_{μ} with that of the deviatoric tensor Λ_{σ} or with that of Λ . Recalling the scalar product for tensors (Eq. [62]), for the diagonalized tensor we have

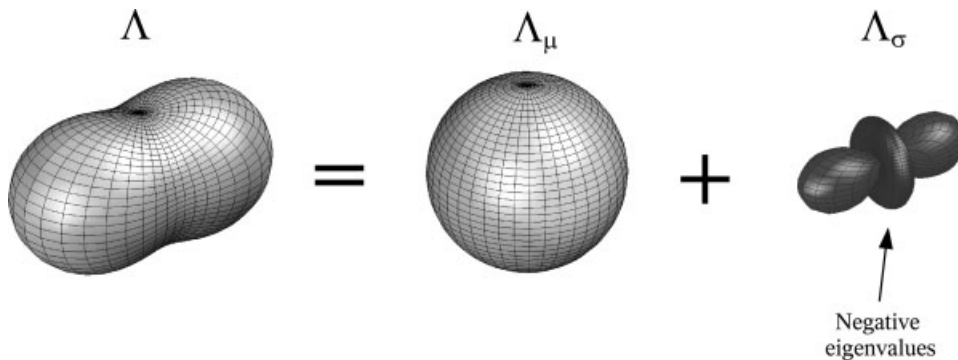


Figure 5 Decomposition of the diagonalised tensor Λ in isotropic Λ_{μ} and deviatoric Λ_{σ} tensors. The deviatoric tensor may have negative eigenvalues. Anisotropy can be measured comparing the magnitude of the deviatoric tensor Λ_{σ} with that of the diagonalised tensor Λ , or with that of the isotropic tensor Λ_{μ} . The surfaces in this figure correspond to diffusivity.

$$\sqrt{\mathbf{\Lambda} : \mathbf{\Lambda}} = \sqrt{\sum_{i=1}^3 \sum_{j=1}^3 \Lambda_{ij}^2} = \sqrt{\lambda_1^2 + \lambda_2^2 + \lambda_3^2}. \quad [72]$$

For the isotropic tensor, we have (14, 48)

$$\sqrt{\mathbf{\Lambda}_\mu : \mathbf{\Lambda}_\mu} = \sqrt{3\langle\lambda\rangle^2} = \sqrt{3}\langle\lambda\rangle. \quad [73]$$

For the deviatoric tensor, we have

$$\sqrt{\mathbf{\Lambda}_\sigma : \mathbf{\Lambda}_\sigma} = \sqrt{(\lambda_1 - \langle\lambda\rangle)^2 + (\lambda_2 - \langle\lambda\rangle)^2 + (\lambda_3 - \langle\lambda\rangle)^2}; \quad [74]$$

it is easily seen that $(\mathbf{\Lambda}_\sigma : \mathbf{\Lambda}_\sigma)$ is three times the variance of the eigenvalues, that is

$$\sqrt{\mathbf{\Lambda}_\sigma : \mathbf{\Lambda}_\sigma} = \sqrt{3\sigma^2} = \sqrt{3}\sigma, \quad [75]$$

where σ is the standard deviation of the distribution of eigenvalues (14, 48).

In order to obtain a metric of anisotropy, the magnitude of the deviatoric tensor $\mathbf{\Lambda}_\sigma$ can be compared with that of the isotropic tensor $\mathbf{\Lambda}_\mu$, leading to the definition of *relative anisotropy* (RA), (14, 48)

$$\begin{aligned} RA &= \frac{\sqrt{\mathbf{\Lambda}_\sigma : \mathbf{\Lambda}_\sigma}}{\sqrt{\mathbf{\Lambda}_\mu : \mathbf{\Lambda}_\mu}} = \frac{1}{\sqrt{3}} \frac{\sqrt{\mathbf{\Lambda}_\sigma : \mathbf{\Lambda}_\sigma}}{\langle\lambda\rangle} \\ &= \frac{1}{\sqrt{3}} \frac{\sqrt{(\lambda_1 - \langle\lambda\rangle)^2 + (\lambda_2 - \langle\lambda\rangle)^2 + (\lambda_3 - \langle\lambda\rangle)^2}}{\langle\lambda\rangle}. \end{aligned} \quad [76]$$

Alternatively, the magnitude of the deviatoric tensor $\mathbf{\Lambda}_\sigma$ can be compared with that of the diagonalised tensor $\mathbf{\Lambda}$, leading to the definition of *fractional anisotropy* (FA) (14, 48),

$$\begin{aligned} FA &= \sqrt{\frac{3}{2}} \frac{\sqrt{\mathbf{\Lambda}_\sigma : \mathbf{\Lambda}_\sigma}}{\sqrt{\mathbf{\Lambda} : \mathbf{\Lambda}}} \\ &= \sqrt{\frac{3}{2}} \sqrt{\frac{(\lambda_1 - \langle\lambda\rangle)^2 + (\lambda_2 - \langle\lambda\rangle)^2 + (\lambda_3 - \langle\lambda\rangle)^2}{\lambda_1^2 + \lambda_2^2 + \lambda_3^2}}. \end{aligned} \quad [77]$$

In isotropic media, $\mathbf{\Lambda}_\sigma : \mathbf{\Lambda}_\sigma = 0$, therefore $FA = 0$ and $RA = 0$; we also note that

$$\begin{aligned} \lim_{\lambda_2, \lambda_3 \rightarrow 0} FA &= \sqrt{\frac{3}{2}} \sqrt{\frac{\lambda_1^2 \left(\left(1 - \frac{1}{3}\right)^2 + \left(-\frac{1}{3}\right)^2 + \left(-\frac{1}{3}\right)^2 \right)}{\lambda_1^2}} \\ &= 1. \end{aligned} \quad [78]$$

Since it can be shown and it is found experimentally that FA is less sensitive to eigenvalue noise than is RA, FA is nowadays more commonly used (49).

The denser an axonal bundle, the more membranes and myelin hinder and restrict diffusion transversally, rendering diffusion more anisotropic: as a consequence, diffusion anisotropy is considered as a rough index of axonal density. To the extent to which denser bundles are assumed to imply stronger anatomical connectivity, anisotropy may be considered as an indicator of connection strength (14, 48, 50).

Visualizing the direction of the principal eigenvector \mathbf{e}_1 can convey useful information on the layout of fiber bundles. Besides rendering ellipsoids or other solids in three dimensions, or using direction field plots, one can assign each video channel to a component of \mathbf{e}_1 (5, 51). In particular, it is conventional to have the orientation of \mathbf{e}_1 control hue and anisotropy control brightness, as in

$$\begin{aligned} \text{Red} &= |\mathbf{e}_{1,x}| \cdot FA, \\ \text{Green} &= |\mathbf{e}_{1,y}| \cdot FA, \\ \text{Blue} &= |\mathbf{e}_{1,z}| \cdot FA. \end{aligned} \quad [79]$$

The corresponding color-map is represented in Fig. 6 (51).

Some examples of the images which can be obtained with DTI are provided in Fig. 7.

It is instructive to discuss how the shape of the ellipsoid varies with the eigenvalues $\lambda_1, \lambda_2, \lambda_3$: since $\lambda_1 > \lambda_2 > \lambda_3$, it can be that $\lambda_1 \gg \lambda_2 \approx \lambda_3$, or $\lambda_1 \approx \lambda_2 \gg \lambda_3$, or $\lambda_1 \approx \lambda_2 \approx \lambda_3$. As depicted in Fig. 8, in the first case the corresponding ellipsoid is *prolate*, that is, it assumes a peanut-like shape. In the second case, the ellipsoid is *oblate*, that is, it assumes a pan-cake-like shape. In the third case, it resembles a sphere.

It is useful to quantify the degree of “prolateness,” “oblateness,” and “sphericity”: as introduced by Westin et al., we can define

$$\begin{aligned} c_1 &= \frac{\lambda_1 - \lambda_2}{\lambda_1} \\ c_p &= \frac{\lambda_2 - \lambda_3}{\lambda_1} \\ c_s &= \frac{\lambda_3}{\lambda_1}, \end{aligned} \quad [80]$$

where c_1 is known as *linear index* (LI), c_p is known as *planar index* (PI), and c_s is known as *spherical index* (SI) (52). The linear index represents the extent to which the shape of an ellipsoid resembles that expected for a single fiber, while the planar index represents the extent to which it resembles that expected for two fibers: examples of the resulting maps are provided in Fig. 9 (52).

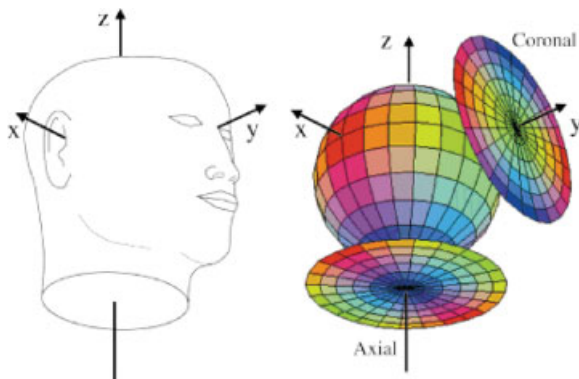


Figure 6 Convention for DTI colour-coding. (Reproduced from (51) with permission from John Wiley & Sons.) Red corresponds to laterolateral, green to dorsoventral (i.e., antero-posterior), and blue to rostro-caudal (i.e., head-feet). [Color figure can be viewed in the online issue, which is available at www.interscience.wiley.com.]

As discussed in the next section, in a typical brain diffusion MRI experiment a considerable number of voxels contain multiple fibers with heterogeneous orientation, a condition usually referred to as *intra-voxel orientational heterogeneity* (IVOH) (53). Since rank-2 tensors can represent only a single directional diffusivity maximum, least-squares fitting results in oblate-shaped ellipsoids when more than one directional orientation is present: in such a case, the direction of the principal eigenvector \mathbf{e}_1 conveys no useful information, and anisotropy indexes from rank-2 tensors are no longer valid indicators of axonal density (50, 53–55).

V. DIFFUSION IN MULTIPLE COMPARTMENTS: THE BIEXPONENTIAL AND GAUSSIAN MIXTURE MODELS

In a typical MRI experiment, voxel size can be between two and three orders of magnitude larger than cell bodies and axonal diameter. As a consequence, voxels contain a combination of intra- and extracellular compartments. Also, they can contain multiple fibres with heterogeneous orientation. We shall discuss the two aspects separately.

Let us begin with the first one. A fraction f of volume corresponds to intracellular spaces. Recalling the first section, we have $D_e > D_i$, where D_e and D_i represent, respectively, intrinsic diffusivity in the extra- and intracellular compartments.

Modeling signal with

$$s = f \exp(-bD_s) + (1 - f) \exp(-bD_f), \quad [81]$$

where D_s and D_f represent slow and fast diffusion components such that $D_f > D_s$, we have

$$\lim_{\Delta \rightarrow 0} s = f \exp(-bD_i) + (1 - f) \exp(-bD_e); \quad [82]$$

this is known as the *biexponential* model (56).

It is tempting to expect to the relationships $D_s = D_i$ and $D_f = D_e$ to hold in general. This would embody several assumptions: that the spin-spin relaxation rate and the concentration of water molecules are equal for the two compartments, that diffusion is Gaussian, that there is no exchange between the two compartments, and that the relaxivity of

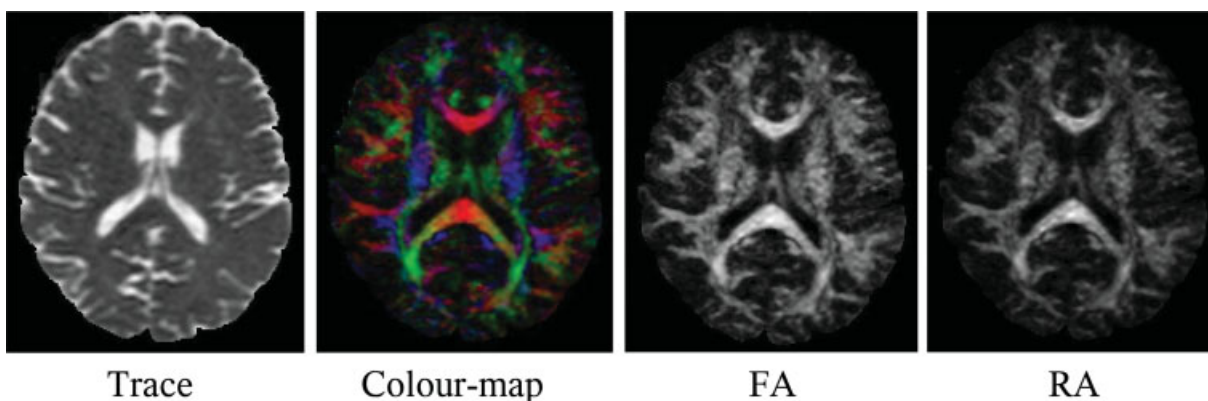


Figure 7 Trace, colourmap, FA, and RA images of an axial brain section. Diffusivity in the brain parenchyma is relatively homogeneous. The genu and splenium of the corpus callosum appear red on the colourmap and highly anisotropic on the FA and RA maps; the corticospinal tract appears blue on the colourmap. From data acquired on a healthy volunteer at 1.5T at Helimed diagnostic imaging sp. z o.o. (Katowice, Poland). [Color figure can be viewed in the online issue, which is available at www.interscience.wiley.com.]

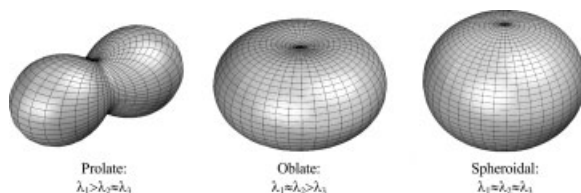


Figure 8 Oblate, prolate and spheroidal ellipsoids. Oblate tensors enable to infer the orientation of a coherently-oriented bundle of axons, prolate tensors occur when orientational heterogeneity is present and only convey planar information, spheroidal tensors do not convey any orientational information. Since the surfaces in this figure correspond to diffusivity, the prolate rank-2 tensor appears peanut-shaped.

membranes is negligible. While the general validity of these assumptions is limited, as shown in Fig. 10 it is found that Eq. [81] fits very well experimental data beyond short diffusion times, accounting for deviations from the exponential model which are observed at intermediate and large b -values.

Fitting measurements taken at achievable diffusion times gives values of D_{slow} in the range of $(0.2\text{--}0.5) \times 10^{-2} \text{ mm}^2 \text{ s}^{-1}$, in good agreement with reported values for intracellular diffusivity; it also gives values of D_{fast} in the range $(1.0\text{--}1.6) \times 10^{-2} \text{ mm}^2 \text{ s}^{-1}$, in agreement with theoretical predictions taking into account the tortuosity of extracellular space (40, 57). Furthermore, it has been shown that under ischemic conditions f_{slow} increases macroscopically (56). Although these findings would suggest a correspondence between D_s and D_f and the intra- and extracellular compartments, the model

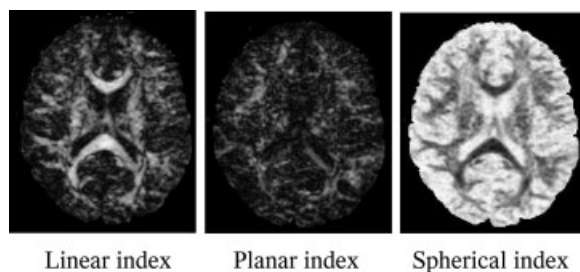


Figure 9 Linear (c_l), planar (c_p) and spherical (c_s) coefficient maps for the same section shown in Fig. 7. The genu and splenium of the corpus callosum are associated with high c_l and low c_p and c_s . Subcortical regions characterised by IVOH are associated with higher c_p and lower c_l . Cortical grey matter is associated with low c_l and c_p and high c_s . From data acquired on a healthy volunteer at 1.5T at Helimed diagnostic imaging sp. z o.o. (Katowice, Poland).

gives $f \approx 0.2$, which is incompatible with known anatomy, from which one knows that $f \approx 0.8$. This discrepancy highlights that simple interpretation of D_s and D_f in terms of D_i and D_e is generally not possible; therefore, beyond the $\Delta \rightarrow 0$ limit the biexponential model becomes essentially a phenomenological one (57).

The confounding effect of differences in spin–spin relaxation rate between the intra- and extracellular compartments has been found to be negligible (56, 58). It has been shown that at short diffusion times the two exponential components are related to two apparent populations of water molecules, corresponding to those that are distant from membranes, and to those that are likely to interact with membranes during the diffusion time, which are associated with reduced apparent diffusivity and increased relaxivity (22, 59). At long diffusion times, biexponential decay arises as diffraction peaks, discussed in the seventh section, disappear due to medium heterogeneity and membrane permeability, leading to an apparent quasi two-compartment behavior (60, 61).

In fact, Schwarcz et al. reported that, since biexponential decay is present in the cold-injured brain parenchyma after massive membrane disintegration, and in centrifuged erythrocyte samples characterized by a negligible extracellular space and no intracellular organelles, compartmentalization is not a prerequisite for its presence (62).

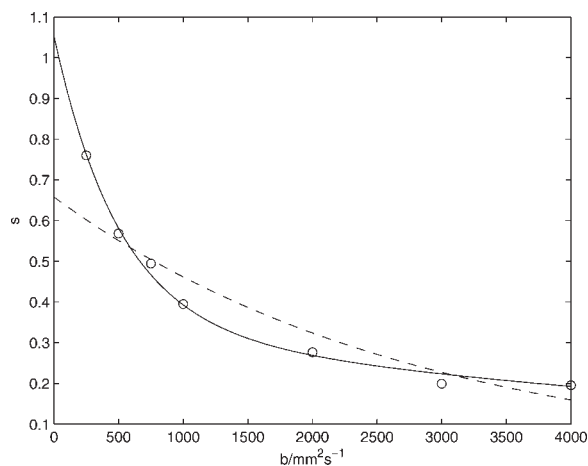


Figure 10 Signal decay from a white matter voxel. The empty circles represent measurements, the dashed line corresponds to exponential fitting (with $D = 0.4 \times 10^{-3} \text{ mm}^2 \text{ s}^{-1}$), the solid line corresponds to biexponential fitting (with $D_{\text{slow}} = 0.1 \times 10^{-3} \text{ mm}^2 \text{ s}^{-1}$, $D_{\text{fast}} = 2.0 \times 10^{-3} \text{ mm}^2 \text{ s}^{-1}$, and $f_{\text{slow}} = 0.33$). The biexponential model fits the measurements considerably better than a single exponential.

Using Eq. [45], we can write

$$D(b) = -\frac{1}{b} \ln[f \exp(-bD_s) + (1-f) \exp(-bD_f)]; \quad [83]$$

from which

$$\lim_{b \rightarrow \infty} \left(-\frac{1}{b} \ln[f \exp(-bD_s) + (1-f) \exp(-bD_f)] \right) = D_s \quad [84]$$

and

$$\lim_{b \rightarrow 0} \left(-\frac{1}{b} \ln[f \exp(-bD_s) + (1-f) \exp(-bD_f)] \right) = fD_s + (1-f)D_f. \quad [85]$$

These limits show that, assuming a biexponential model of signal decay, the diffusivity measured from two points depends on the b -value as a consequence of the nonlinear function with which diffusivities are combined: it decreases as the b -value is increased.

Let us now turn to the case of multiple fiber orientations within a voxel.

Such a situation may originate from a number of topologies: an interface between adjacent axonal bundles occupying the same voxel due to partial voluming, an actual crossing of the axonal matrices of multiple bundles, or a single bundle spreading or narrowing with a fan-like structure (50, 63).

In order to explore the properties of diffusion in a voxel containing multiple fibers with heterogeneous orientation (a condition referred to as IVOH, as defined in the previous section), let us consider an orthogonal crossing of two bundles, “a” and “b”, aligned, respectively, parallel to the x and y axes. Let the corresponding diffusion tensors be \mathbf{D}_a and \mathbf{D}_b , and the corresponding ensemble average diffusion propagators be $P_a(\mathbf{R}, \tau)$ and $P_b(\mathbf{R}, \tau)$.

If f and $(1-f)$ are the volume fractions corresponding to the two bundles, the probability for a randomly chosen water molecule to undergo a displacement \mathbf{R} can be written as

$$P(\mathbf{R}, \tau) = fP_a(\mathbf{R}, \tau) + (1-f)P_b(\mathbf{R}, \tau). \quad [86]$$

Figure 11 shows the plot of displacement probability as a function of direction, for a given displacement $|\mathbf{R}|$ and time interval τ ; the axes have arbitrary units. It can be seen that the maxima of displacement probability correspond to the directions of orientation of the fiber bundles (34, 64).

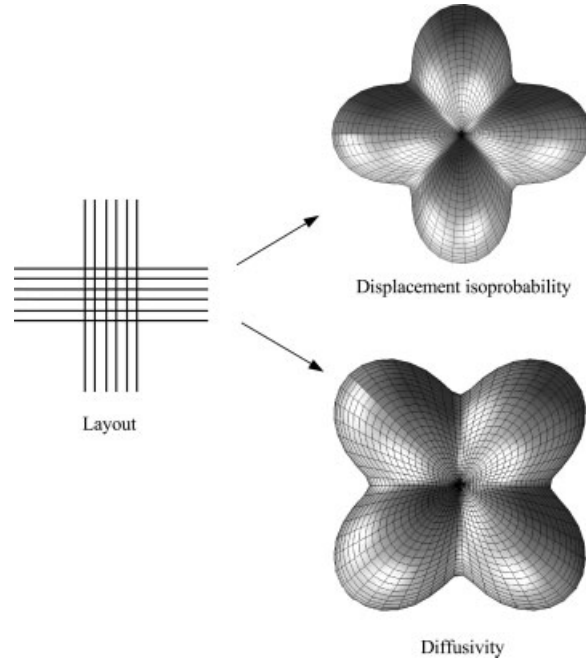


Figure 11 Displacement isoprobability and diffusivity as a function of direction. Example for $\mathbf{e}_{1a} = (1,0,0)^T$, $\mathbf{e}_{2a} = (0,1,0)^T$, $\lambda_1 > \lambda_2 = \lambda_3$ for both tensors, $f = 1/2$, and arbitrary b and τ . Displacement isoprobability maxima correspond to bundle orientation, diffusivity maxima do not. This is a consequence of the fact that diffusivities are combined with a nonlinear function (Eq. [88]), while displacement probabilities are combined with a linear function (Eq. [86]).

Assuming that signal adds independently, we can write

$$s(\mathbf{g}, b) = f \exp(-b\mathbf{g}^T \mathbf{D}_a \mathbf{g}) + (1-f) \exp(-b\mathbf{g}^T \mathbf{D}_b \mathbf{g}), \quad [87]$$

from which

$$D(\mathbf{g}, b) = -\frac{1}{b} \ln[f \exp(-b\mathbf{g}^T \mathbf{D}_a \mathbf{g}) + (1-f) \exp(-b\mathbf{g}^T \mathbf{D}_b \mathbf{g})]. \quad [88]$$

Figure 11 shows the plot of measured diffusivity $D(\mathbf{g}, b)$ as a function of direction for a given b -value; the axes have arbitrary units. It is evident that, when IVOH is present, diffusivity maxima no longer correspond to the directions of orientation of the fiber bundles (53). This is a consequence of the nonlinear function with which diffusivities are combined, as opposed to the sum with which displacement probabilities are combined (Eq. [86]). The relationship between angular diffusivity pattern and underlying

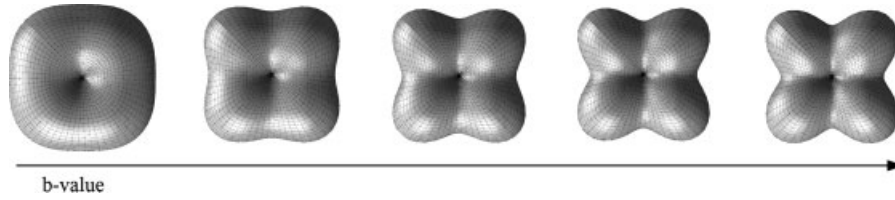


Figure 12 Relationship between angular diffusivity pattern and b -value. Low b -values do not enable to resolve multiple fibres; while the diffusivity maxima remain unaltered, the minima become deeper as the b -value is increased, resulting in improved contrast. For $b \rightarrow 0$, the diffusivity pattern becomes round on the crossing plane.

layout, although simple for this example with orthogonally crossing fibers, is generally complex, and has been solved analytically only recently (64).

It is instructive to explore how $D(\mathbf{g}, b)$ varies with the b -value. We note that for a direction \mathbf{g} such that $\mathbf{g}^T \mathbf{D}_a \mathbf{g} = \mathbf{g}^T \mathbf{D}_b \mathbf{g}$ Eq. [88] simplifies to

$$D(\mathbf{g}, b) = \mathbf{g}^T \mathbf{D}_a \mathbf{g} = \mathbf{g}^T \mathbf{D}_b \mathbf{g}. \quad [89]$$

For different direction \mathbf{g}' , let $\mathbf{g}'^T \mathbf{D}_a \mathbf{g}' < \mathbf{g}'^T \mathbf{D}_b \mathbf{g}'$, we have

$$\lim_{b \rightarrow \infty} \left(-\frac{1}{b} \ln [f \exp(-b \mathbf{g}'^T \mathbf{D}_a \mathbf{g}') + (1-f) \exp(-b \mathbf{g}'^T \mathbf{D}_b \mathbf{g}')] \right) = \mathbf{g}'^T \mathbf{D}_a \mathbf{g}', \quad [90]$$

which is akin to the limit in Eq. [84]. As represented in Fig. 12 for the layout from Fig. 11, the contrast between the two fibers improves with increasing b -value; the effect is clearly not specific to the case of two orthogonally crossing fibers. As a consequence, large b -values, such that $\exp(-bD)$ cannot be truncated to $1 - bD$, are needed to resolve multimodal diffusion.

Equation [87] can be extended to n fiber bundles

$$s(\mathbf{g}, b) = \sum_{i=1}^n f_i \exp(-b \mathbf{g}^T \mathbf{D}_i \mathbf{g}), \quad [91]$$

where f_i and \mathbf{D}_i are the volume fractions and diffusion tensors corresponding to the bundles. This is known as the *Gaussian mixture model*; while diffusion is assumed to be Gaussian along all directions, no restriction is placed on the angular pattern. Also, it is assumed that there is no exchange among fibers, so that signal adds independently (53).

Because of the presence of the sum of exponentials, a linear relationship between $D(\mathbf{g}, b)$ and the

elements of \mathbf{D}_i cannot be established, hence the least squares method cannot be applied as in Eq. [60]. The determination of \mathbf{D}_i must therefore be treated as an optimization problem, searching in a space with $(7n - 1)$ dimensions (i.e. for each fiber, six degrees of freedom corresponding to the tensor elements and one corresponding to its volume fraction).

The measurement of diffusivity along a large number of noncollinear directions is often referred to as *high angular resolution diffusion imaging* (HARDI).

It has been determined experimentally that fitting Eq. [91] to noisy data is unstable for $n > 2$, and that multiple restarts are necessary in order to obtain reliable fitting for $n = 2$ (corresponding to Eq. [87]) (53, 65, 66).

It is instructive to note two facts about Eq. [91]. First, it enables to determine the volume fractions of the bundles. Second, n has to be assumed a priori; it can be determined by means of probabilistic methods (53, 65, 66). The fact that a discrete number of orientations is assumed is an important limitation, since in the brain IVOH is frequently induced by the presence of fan-like layouts, which cannot be adequately described by a finite number of orientations.

While for brevity this section covered the biexponential and Gaussian mixture models only, more advanced models do exist. For example, in 2004 Assaf et al. introduced a composite model of hindered and restricted diffusion, known as CHARMED, in which hindered diffusion is characterized by an effective diffusion tensor and restricted diffusion is described by means of the q -space formalism, introduced in the seventh section; although this model enables more accurate determination of fiber orientation, the volume fraction discrepancy remains (67). Analytical modeling of diffusion in the bovine optic nerve, representing restricted diffusion within axons and glial cells by means of ellipsoidal and spheroidal compartments and accounting for membrane permeability, resulted in more realistic predictions of

microstructural parameters, albeit with limited goodness of fit (68).

VI. GENERALISED DIFFUSION TENSOR IMAGING

In order to remove the limitations stemming from the inability of the rank-2 tensor model to represent multimodal diffusion in presence of IVOH one may consider higher-order diffusion tensors, as an alternative to the Gaussian mixture model introduced in the previous section.

A rank- l (or, equivalently, an order- l) tensor is a multidimensional array with l dimensions, of which scalars ($l = 0$), vectors ($l = 1$) and matrices ($l = 2$) are special cases.

The rank-2 tensor introduced in Eq. [11] has a mathematical precursor, the *dyad product*, which can be written as

$$\mathbf{B} = \mathbf{u} \circ \mathbf{v}, \quad [92]$$

where \circ is the outer product, and \mathbf{u} and \mathbf{v} are vectors; this is equivalent to

$$B_{ij} = u_i v_j, \quad [93]$$

for $i, j = 1, 2, 3$ (69).

Equations [92] and [93] have a natural generalization for $l > 2$; for instance, for $l = 4$ we have

$$\mathbf{D} = \mathbf{u} \circ \mathbf{v} \circ \mathbf{w} \circ \mathbf{x}, \quad [94]$$

and

$$D_{ijklm} = u_i v_j w_k x_m, \quad [95]$$

for $i, j, k, m = 1, 2, 3$ (69).

Clearly, for $l > 2$ tensors cannot be represented by matrices: these are frequently referred to as *higher-order* (or, equivalently, *rank*) *tensors*.

Although diagonalization is not defined for $l > 2$, generalized forms of the SVD (Eq. [67]) do exist: the PARAFRAC decomposition,

$$\mathbf{D} = \sum_{i=1}^3 \sigma_{iiii} \mathbf{u}_i \circ \mathbf{v}_i \circ \mathbf{w}_i \circ \mathbf{x}_i, \quad [96]$$

and the Tucker decomposition,

$$\mathbf{D} = \sum_{i=1}^3 \sum_{j=1}^3 \sum_{k=1}^3 \sum_{m=1}^3 \sigma_{ijkl} \mathbf{u}_i \circ \mathbf{v}_j \circ \mathbf{w}_k \circ \mathbf{x}_m, \quad [97]$$

given here for $l = 4$. The former is unique, and yields a diagonal $\boldsymbol{\sigma}$, corresponding to the diagonal eigen-

value matrix in Eq. [67]; the latter is not unique, but yields orthogonal $\mathbf{u}_i, \mathbf{v}_j, \mathbf{w}_k, \mathbf{x}_m$ (46, 70, 71).

Although higher-order tensors have no obvious geometrical or physical analogy, they are a useful formalism for describing deviation from the anisotropic Gaussian propagator (Eq. [23]). Two models have been proposed: one (sometimes referred to as GDTI-2), introduced by Ozarslan et al., preserves the assumption of the radial components of the propagator being Gaussian, the other one (sometimes referred to as GDTI-1), introduced by Liu et al., does not (72, 73).

Let us begin exploring the first one, and consider that for $l = 2$ we can write

$$D(\mathbf{g}) = \mathbf{g}^T \mathbf{D} \mathbf{g} = \sum_{i=1}^3 \sum_{j=1}^3 D_{ij} g_i g_j, \quad [98]$$

which, as discussed in Ref. (72), has a natural generalization for rank l :

$$D(\mathbf{g}) = \sum_{i_1=1}^3 \sum_{i_2=1}^3 \cdots \sum_{i_l=1}^3 D_{i_1 i_2 \cdots i_l} g_{i_1} g_{i_2} \cdots g_{i_l}, \quad [99]$$

where $D_{i_1 i_2 \cdots i_l}$ are the elements of a rank- l tensor. Analogously to the Gaussian mixture model, while embodying the assumption that diffusion along any direction is Gaussian and therefore maintaining the use of the diffusion coefficient, Eq. [99] does not place any restriction on the angular pattern (72).

The angular pattern represented by a higher-order tensor can be visualized by means of a geometrical analogy, provided by considering the surface parameterized by

$$\psi(\theta, \phi) = D \begin{pmatrix} \cos(\phi) \cos(\theta) \\ \cos(\phi) \sin(\theta) \\ \sin(\phi) \end{pmatrix}, \quad [100]$$

which is defined over the unit sphere; for $l = 2$, this corresponds to an ellipsoid (Eq. [68]).

As diffusion is antipodally symmetric, one needs $D(\mathbf{g}) = D(-\mathbf{g})$; this condition is met using even rank tensors.

As a consequence of the fact that multiplication is commutative

$$D_{i_1 i_2 \cdots i_l} = D_{(i_1 i_2 \cdots i_l)}, \quad [101]$$

where (\dots) is the permutation operator; a rank- l diffusion tensor therefore has

$$N(l) = \frac{(l+1)(l+2)}{2} \quad [102]$$

unique elements. For example, $N(2) = 6$, $N(4) = 15$, and $N(6) = 28$; the multiplicity of each element is given by

$$\mu = \frac{l!}{n_x!n_y!n_z!}, \quad [103]$$

where n_x, n_y, n_z correspond to the number of times each unit vector appear corresponding to the element (69, 72).

As rank is increased the ability to reproduce complex multimodal angular patterns improves; this is well-evident in the examples for one, two, and three fibers and $l = 2, 4, 6$ shown in Fig. 13 (50, 72).

Least-squares fitting of the diffusion tensor (Eq. [60]) can be easily generalized to arbitrary rank, taking into account the multiplicity of each element and rearranging the tensor elements in a vector; for example, for $l = 4$ and the linear system $\mathbf{Ax} = \mathbf{b}$,

$$\begin{aligned} \mathbf{a}_i &= (x^4, y^4, z^4, 4x^3y, 4x^3z, 4y^3x, 4y^3z, 4z^3x, \dots, 4z^3y, 6x^2y^2, 6x^2z^2, 6y^2z^2, 12x^2yz, 12y^2xz, 12z^2xy), \\ \mathbf{x} &= (D_{xxxx}, D_{yyyy}, D_{zzzz}, D_{xxyy}, D_{xxzz}, D_{yyxx}, D_{yyzz}, \dots, D_{zzzx}, D_{zzzy}, D_{xxyy}, D_{xxzz}, D_{yyzz}, D_{xxyy}, D_{yyxz}, D_{zzxy})^T, \\ \mathbf{b} &= (-1/b \ln(s_1) \dots - 1/b \ln(s_i) \dots - 1/b \ln(s_N))^T, \end{aligned} \quad [104]$$

where \mathbf{a}_i are the row vectors of the matrix \mathbf{A} , and $i = 1, \dots, N$ (72).

Interestingly, as proposed by Ozarslan et al., the eigenvalue variance-based metrics of anisotropy (FA and RA, Eqs. [76] and [77]) can be generalized to higher-order tensors. Unitless variance of the normalized diffusivity can be written as

$$V = \langle D_N(\mathbf{g})^2 \rangle - \langle D_N(\mathbf{g}) \rangle^2, \quad [105]$$

where (74)

$$D_N(\mathbf{g}) = \frac{D(\mathbf{g})}{\langle D(\mathbf{g}) \rangle}. \quad [106]$$

Since $\lim_{l \rightarrow \infty} \sup(V) = \infty$, it is convenient to remap the interval $[0, \infty)$ to $[0, 1)$, leading to the definition of *generalized anisotropy* (GA):

$$GA = 1 - \frac{1}{1 + (k_1 V)^{\epsilon(V)}}, \quad [107]$$

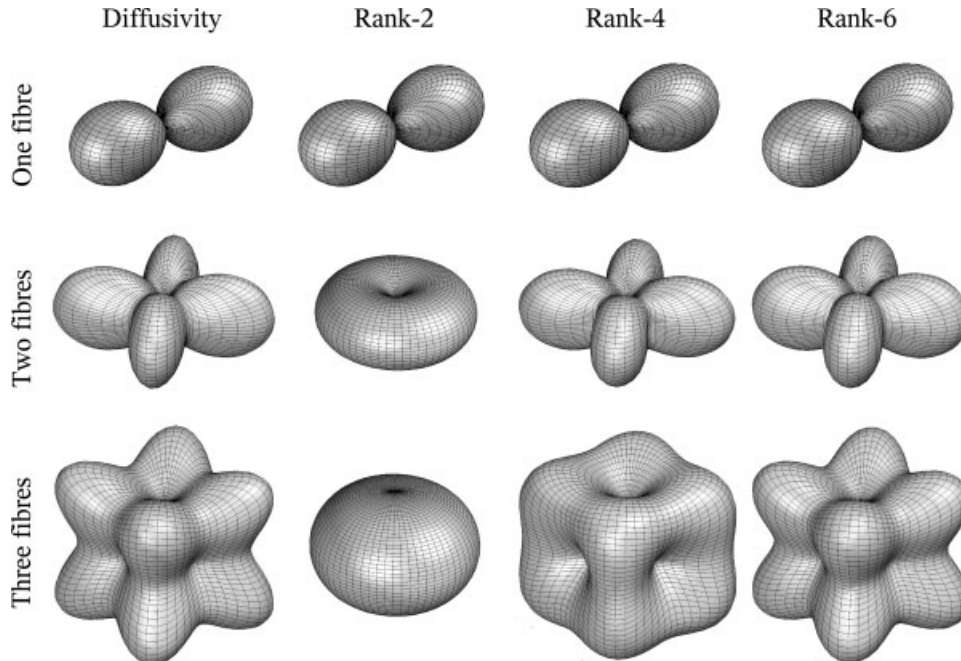


Figure 13 Effect of tensor rank on reconstruction of multimodal diffusivity patterns. (Reproduced from (50) with permission from John Wiley & Sons.) The rank-2 tensor is an accurate representation only for the one-fibre case; it is oblate for the case of two crossing fibres, and spheroidal for the case of three orthogonally crossing fibres. Multiple maxima are revealed elevating rank to four; elevating rank to six removes distortion for the three-fibre case. One should note that the surfaces in this figure correspond to diffusivity (see Eq. [100]).

where the exponent

$$\varepsilon(V) = 1 + \frac{1}{1 + k_2 V}, \quad [108]$$

and where k_1 and k_2 are scaling coefficients (74).

Since $D_N(\mathbf{g})$ is positive, definite and integrates to one, an alternative approach is to consider orientation and not diffusivity as the random variable, and to consider $D_N(\mathbf{g})$ as its PDF:

$$\sigma = -\frac{3}{2\pi} \int_{\Omega} D_N(\mathbf{g}) \ln D_N(\mathbf{g}) d\mathbf{g}, \quad [109]$$

where σ is the differential entropy of the distribution. Since $\lim_{l \rightarrow \infty} \inf(\sigma) = -\infty$, it is convenient to remap the interval $(-\infty, \ln 3)$ to $[0,1)$, leading to the definition of *scaled entropy* (SE):

$$SE = 1 - \frac{1}{1 - (k_3(\ln 3 - \sigma))^{\varepsilon(\ln 3 - \sigma)}}, \quad [110]$$

where k_3 is a scaling coefficient (74).

For $l = 2$, GA is akin to FA. GA and SE are not rank-invariant, and it has been shown both in simulations and on the basis of data acquired in vivo that they increase with rank in regions where IVOH is present (50, 74). Their relative merits remain to be characterized: while from a theoretical viewpoint SE may be preferable since it is not clear why the square of the difference and not any other power should be considered in the definition of GA, from a computational viewpoint GA is preferable since the logarithm in the entropy function forces to resort to numerical integration (74). It is also worthwhile to note that these metrics are valid for any function defined over the unit sphere.

Let us now turn to GDTI-1.

Fick's first law for anisotropic diffusion (Eq. [10]) can be written as

$$J_i = -D_{ij} \frac{\partial C}{\partial x_j} \quad [111]$$

where $i, j = 1, \dots, 3$. As discussed in Ref. (73), the assumption of Gaussian diffusion is embodied in this proportionality relationship, and may be removed by introducing higher-order terms:

$$J_{i_1} = -D_{i_1 i_2} \frac{\partial C}{\partial x_{i_2}} - D_{i_1 i_2 i_3} \frac{\partial^2 C}{\partial x_{i_2} \partial x_{i_3}} - D_{i_1 i_2 i_3 i_4} \frac{\partial^3 C}{\partial x_{i_2} \partial x_{i_3} \partial x_{i_4}} - \dots; \quad [112]$$

analogously, Fick's second law (Eq. [8]) becomes

$$\frac{\partial C}{\partial t} = D_{i_1 i_2} \nabla_{i_1 i_2} C + D_{i_1 i_2 i_3} \nabla_{i_1 i_2 i_3} C + D_{i_1 i_2 i_3 i_4} \nabla_{i_1 i_2 i_3 i_4} C + \dots, \quad [113]$$

which is also known as the *Kramers–Moyal* expansion (73).

Assuming that diffusion is a Markov process, the higher-order tensors can be related to statistics of the random displacement (73).

According to this model, signal attenuation can be written as (73)

$$\ln(s) = -b_{i_1 i_2} D_{i_1 i_2} - ib_{i_1 i_2 i_3} D_{i_1 i_2 i_3} - b_{i_1 i_2 i_3 i_4} D_{i_1 i_2 i_3 i_4} - ib_{i_1 i_2 i_3 i_4 i_5} D_{i_1 i_2 i_3 i_4 i_5} - \dots \quad [114]$$

The magnitude of the signal is determined by the even-order tensors, which represent antipodally symmetric patterns. Its phase is determined by the odd-order tensors, representing antisymmetric patterns, which do not occur unless there is net flux of molecules. Physiological activity corrupts the phase of the signal, forcing to introduce a simplifying assumption setting odd-order tensors to zero, which is equivalent to assuming the flow term in Eq. [30] is null.

GDTI-2, in virtue of the assumption of Gaussianity, does not require measurements to be taken at more than one b -value per direction; this is not the case for GDTI-1, which is associated with long acquisition times determined by the combination of a large number of directions and b -values.

In regions of the brain where fibers are coherently oriented the relationship between anisotropy and axonal density, myelination, and integrity is strong. In regions with a more complex orientational layout, the effect of these factors on anisotropy depends on the degree of orientational coherence and the inability of the rank-2 tensor model to represent multimodal diffusion biases measurements of FA and RA to artifactually low values. Minati et al. have recently shown that elevating rank from 2 to 4 increases GA and SE in subcortical regions of the corona radiata, along the superior longitudinal fasciculus, along the radiations of the genu of the corpus callosum, in peritrigonal white matter and along the inferior frontooccipital and longitudinal fascicula, and also in other regions not affected by IVOH; removing artifactual underestimation of anisotropy, GDTI may provide indexes more realistically representing axonal density and in-

tegrity than FA and RA, thereby potentially increasing sensitivity to pathological change (50).

VII. SPHERICAL HARMONIC DECOMPOSITION AND SPHERICAL DECONVOLUTION

In the tensor decomposition given in the first section, $\mathbf{D} = \mathbf{R}^T \mathbf{\Lambda} \mathbf{R}$ (Eq. [12]), the rotation matrix and the tensor were expressed in Cartesian coordinates $\mathbf{e} = (x, y, z)^T$, since this is a natural choice determined by the gradient system. However, diffusion is more succinctly described in spherical coordinates $\mathbf{e} = (r, \theta, \phi)^T$.

In this section we shall introduce a complete orthonormal basis for functions defined over the unit sphere, the *spherical harmonics* $Y_l^m(\theta, \phi)$, and show that the associated decomposition, analogous to the Fourier transform for spherical coordinates, possesses some properties which are useful to analyze the angular pattern of diffusivity and signal attenuation.

Physicists and mathematicians tend to use different angular conventions for spherical coordinates, and this is a potential source of confusion. We shall follow the physicists' convention and take θ as the colatitudinal or polar coordinate with $0 \leq \theta < \pi$, and ϕ as the longitudinal coordinate with $0 \leq \phi < 2\pi$.

Spherical harmonics $Y_l^m(\theta, \phi)$ are continuous, bounded, complex functions of the angular coordinates θ and ϕ ; introduced by Heine in 1881, they are frequently encountered in physics, for example as eigenfunctions of angular momentum operators in quantum mechanics (75).

They are defined, for order $l = 0, \dots, \infty$ and degree $m = -l, \dots, l$, as

$$Y_l^m(\theta, \phi) = \sqrt{\frac{2l+1}{4\pi} \frac{(l-m)!}{(l+m)!}} P_l^m(\cos \theta) \exp(im\phi), \quad [115]$$

where $P_l^m(x)$ are the Legendre associated polynomials, (75)

$$P_l^m(x) = \frac{(-1)^2}{2^l l!} (1-x^2)^{m/2} \frac{d^{l+m}}{dx^{l+m}} (x^2-1)^l. \quad [116]$$

The spherical harmonics are related to the rotation matrices for spherical tensors, known as *Wigner rotation matrices*, having the form

$$D_{m0}^l(\alpha, \beta, \gamma)^* = \sqrt{\frac{4\pi}{2l+1}} Y_l^m(\beta, \alpha); \quad [117]$$

the elements of the rotation matrices for rank l spherical tensors with second index equal to zero are proportional to the spherical harmonics (76).

For the purpose of decomposing the real-valued diffusivity and signal magnitude functions, we shall use real-valued linear combinations of the complex-valued $Y_l^m(\theta, \phi)$, defined as

$$\begin{aligned} S_l^m(\theta, \phi) &= \frac{1}{\sqrt{2}} (Y_l^m(\theta, \phi) + Y_l^{-m}(\theta, \phi)) \\ S_l^0(\theta, \phi) &= Y_l^0(\theta, \phi) \\ S_l^{-m}(\theta, \phi) &= \frac{1}{i\sqrt{2}} (Y_l^m(\theta, \phi) - Y_l^{-m}(\theta, \phi)), \end{aligned} \quad [118]$$

for order $l = 0, \dots, \infty$ and degree $m = -l, \dots, l$ (75).

As discussed in Ref. (77), these real combinations enable to expand $D(\theta, \phi)$ in a Laplace series,

$$D(\theta, \phi) = \sum_{l=0}^{\infty} \sum_{m=-l}^l a_{lm} S_l^m(\theta, \phi). \quad [119]$$

As shown in Fig. 14, the real combinations of the spherical harmonics have two interesting properties. First, even-order harmonics are antipodally symmetrical, and odd-order harmonics are antisymmetrical. Second, $S_0^0(\theta, \phi)$ corresponds to a sphere, $S_2^m(\theta, \phi)$ for $m = -2, \dots, 2$ have a single directional maximum (i.e., a direction \mathbf{u} for which $D(\mathbf{u}) = D(-\mathbf{u}) = D_{\max}$), $S_4^m(\theta, \phi)$ for $m = -4, \dots, 4$ have two directional maxima, and higher-order harmonics have an increasing angular frequency (77).

The coefficients a_{lm} in Eq. [119] can be determined with

$$a_{lm} = \int_0^{2\pi} \int_0^\pi D(\theta, \phi) S_l^m(\theta, \phi) \sin \theta d\theta d\phi, \quad [120]$$

which is known as the *spherical harmonic decomposition* (SHD), and which is analogous to the Fourier transform in spherical coordinates (77).

When signal magnitude is considered, and the diffusion propagator is therefore assumed to be antipodally symmetric, in the absence of noise all odd-order coefficients are zero. For isotropic diffusion, only a_{00} is non-zero. For monomodal diffusion (i.e., a single fiber) only a_{00} and a_{2m} for $m = -2, \dots, 2$ are nonzero, because higher-order harmonics have multiple directional maxima, and it can be shown that their SHD coefficients evaluate to zero for monomodal diffusivity patterns; for

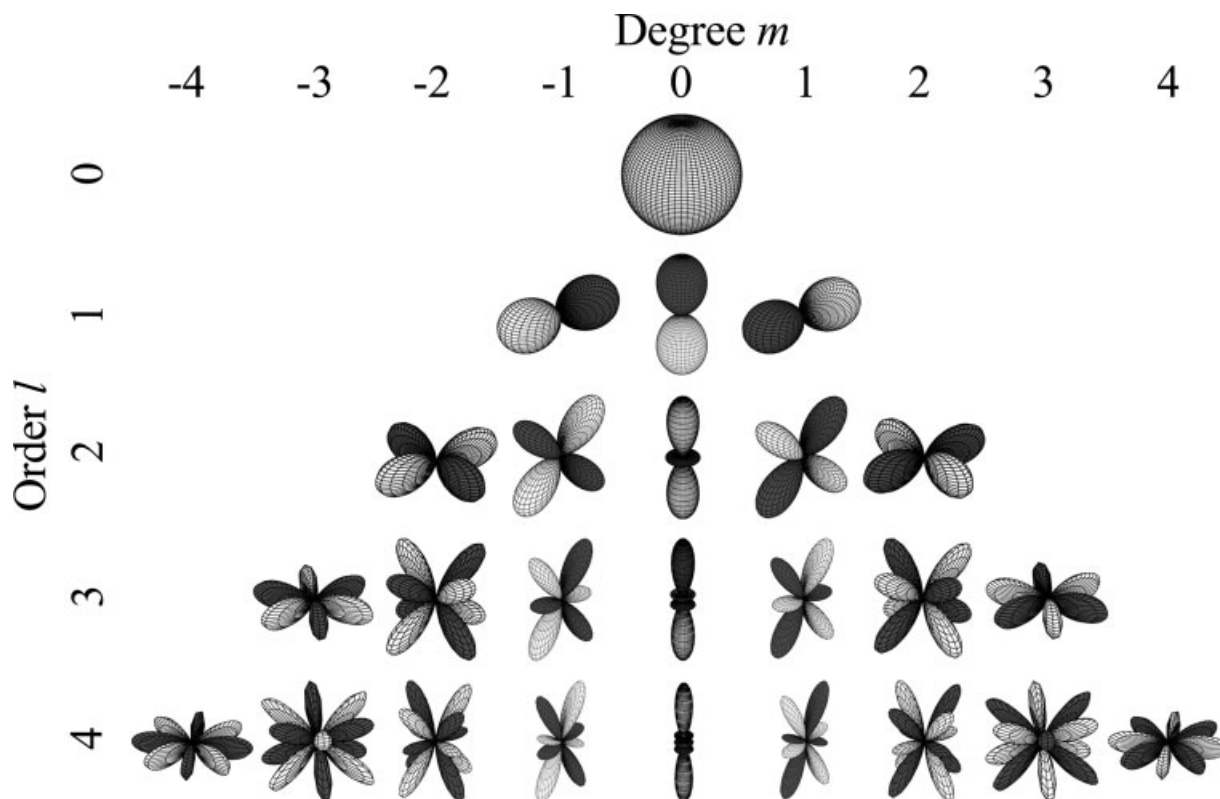


Figure 14 Plots of the real combinations of the spherical harmonics for $l = 0 \dots 4$. Black corresponds to negative values. Even-order harmonics are antipodal symmetric, odd-order harmonics are antisymmetric. The angular frequency increases with order.

multimodal diffusion, the contribution of higher-order terms increases with angular frequency (77).

Direct computation of a_{lm} from Eq. [120] results in a large computational load if interpolation and numerical integration are used, and poor accuracy if integration is replaced by summation. A more convenient approach is computation of a_{lm} in matrix form. Let \mathbf{d} be the vector of diffusivity measurements with $d_i = D(\theta_i, \phi_i)$ for $i = 1, \dots, N$, $j(l, m) = l^2 + l + m$ be a unique integer indexing each spherical harmonic, and \mathbf{h} be the vector of decomposition coefficients with $h_{j(l,m)} = a_{lm}$ for $j = 0, \dots, j(l_{\max}, l_{\max})$. Then one can write

$$\mathbf{h} = (\mathbf{X}^T \mathbf{X})^{-1} \mathbf{X}^T \mathbf{d}, \quad [121]$$

where \mathbf{X} with $X_{ij(l,m)} = S_l^m(\theta_i, \phi_i)$ is a $N \times j(l_{\max}, l_{\max})$ matrix (78).

Spherical harmonics are a convenient basis for interpolation in spherical coordinates; additionally, they enable to remove a fraction of measurement noise by forcing odd-order terms to be null.

It has been shown that for the case of a single fiber the polar and longitudinal angles of the fiber can be

derived from the second-order coefficients a_{2m} for $m = -2, \dots, 2$ (77).

The relationship between harmonic order and angular frequency provides a convenient means to characterize deviation from monomodal diffusion. Writing the signal magnitude for a given harmonic order l as

$$W_D(l) = \sum_{m=-l}^l a_{lm}^2, \quad [122]$$

the *fiber multiplicity index* (FMI) introduced by Frank et al., can be formulated as

$$\text{FMI} = \frac{\sum_l W_D(l)}{W_D(2)}, \quad [123]$$

for even $l \geq 4$ (77).

Equation [123] enables to detect IVOH by thresholding the FMI; an alternative, put forward by Alexander et al., is to use analysis of variance (ANOVA) to assess whether increasing harmonic order significantly changes $D(\theta, \phi)$ reconstructed

from Eq. [119] (78). Zhan et al. reported that maps of $W_D(0)$, $W_D(2)$, and $W_D(4)$ exhibit strong consistency with DTI-derived mean diffusivity $\langle D \rangle$, linear index c_1 and planar index c_p (79).

Another application of SHD is direct reconstruction of fiber orientation by means of spherical deconvolution. Normalized signal $S(\theta, \phi)$ from a population of crossing fibers can be naturally written as a convolution in spherical coordinates

$$S(\theta, \phi) = R(\theta) \otimes F(\theta, \phi), \quad [124]$$

where $F(\theta, \phi)$ is the normalized fiber *orientation density* (or *distribution*) *function* (ODF). Conceptually, $F(\theta, \phi)$ is akin to $\psi(\mathbf{u})$ introduced in the next section, also referred to as ODF, although the two methods will generally give different estimates. $R(\theta)$ is the response function for a single fiber aligned with the z -axis, which is assumed to be axially symmetric (80).

As discussed by Tournier et al., spherical deconvolution can be reduced to a set of matrix operations. Let \mathbf{s}^n be the vector of n th order SHD coefficients for $S(\theta, \phi)$, and \mathbf{f}^n be the vector of n th order SHD coefficients of $F(\theta, \phi)$. Then one can write

$$\mathbf{s}^n = \mathbf{R}^n \mathbf{f}^n, \quad [125]$$

where \mathbf{R}^n is a $(2n + 1)(2n + 1)$ matrix, representing the n th order rotational harmonic decomposition of $R(\theta)$. The SHD coefficients of $F(\theta, \phi)$ can therefore be obtained by inverting \mathbf{R}^n . Since $F(\theta, \phi)$ is antipodally symmetric, only even orders have to be considered; $R(\theta)$ can be estimated directly from a high-anisotropy voxel, assuming that it does not differ among bundles (80).

VIII. DSI AND Q-BALL IMAGING: THE FOURIER RELATIONSHIP AND THE FUNK-RADON TRANSFORM

Let us recall Eq. [49], which establishes that for a population of spins and a diffusion time τ

$$c(q, \tau) = \mathfrak{F}[P(X, \tau)], \quad [126]$$

where $q = \gamma g \delta$, and where the right-hand side is the Fourier transform of the one-dimensional propagator $P(X, \tau)$.

The relationship between displacement and dephasing, expressed in Eq. [33] for one dimension, can be extended to three dimensions:

$$\phi = \gamma \int_0^\delta \mathbf{g} \cdot \mathbf{r} dt - \gamma \int_\Delta^{\Delta+\delta} \mathbf{g} \cdot \mathbf{r}' dt = \gamma \delta \mathbf{g} \cdot \mathbf{R}, \quad [127]$$

where $\mathbf{R} = \mathbf{r}' - \mathbf{r}$, and where, as a consequence of the SGP condition, \mathbf{g} and \mathbf{r} are time-independent vectors.

Since the Larmor relationship is linear, the dephasing PDF $p(\phi)$, corresponding to $P(X, \tau)$ in one dimension, corresponds to $P(\mathbf{R}, \tau)$ in three dimensions; it follows that the Fourier relationship can be naturally extended to

$$c(\mathbf{q}, \tau) = \int \exp(i\mathbf{q} \cdot \mathbf{R}) P(\mathbf{R}, \tau) d\mathbf{R} = \mathfrak{F}[P(\mathbf{R}, \tau)], \quad [128]$$

where $\mathbf{q} = \gamma \delta \mathbf{g}$ is known as the *reciprocal space vector* (16, 21, 81).

Reconstruction of $P(\mathbf{R}, \tau)$ is possible by means of the inverse Fourier transform of the complex signal measured at a diffusion time τ (one should note that in this context $+i$ is used for \mathfrak{F} and $-i$ for \mathfrak{F}^{-1}),

$$P(\mathbf{R}, \tau) = \int \exp(-i\mathbf{q} \cdot \mathbf{R}) c(\mathbf{q}, \tau) d\mathbf{q} = \mathfrak{F}^{-1}[c(\mathbf{q}, \tau)], \quad [129]$$

which is free from a priori assumptions about the propagator (26, 27).

If the EAP is antipodally symmetric, that is, if there is no net flux of molecules, imaginary terms in the Fourier transform sum up to zero; in this case, when ensemble average signal is considered, neglecting the effect of noise no information is lost by taking signal magnitude $s = |c|$ (34)

$$P(\mathbf{R}, \tau) = \mathfrak{F}^{-1}[s(\mathbf{q}, \tau)]. \quad [130]$$

Equation [127] in its current form holds outside the SGP condition if \mathbf{R} is considered as δ -averaged displacement, and $P(\mathbf{R}, \tau)$ as the *centre-of-mass propagator* (26, 27). It has been shown experimentally that this results in underestimation of displacement; varying δ from 4.5 to 72 ms was reported by Assaf et al. to result in net displacement changing by a factor of about 2 (28).

If the SGP condition is met and the complex signal is considered, reconstruction of $P(\mathbf{R}, \tau)$ by means of the Fourier transform is referred to as QSI, otherwise it is referred to as DSI; due to gradient slew-rate limitations and phase contamination, only DSI can be applied in vivo (34, 61).

Two forms of QSI/DSI are possible: three-dimensional reconstruction of the whole propagator with Eq. [129] from measurements taken on a Cartesian lattice, and one-dimensional reconstruction of individual radial components of the propagator along

each sampling direction with Eq. [126]; clearly, in both cases the measured displacement PDF depends on the diffusion time τ (61, 82).

In a QSI/DSI experiment the hardware resolution is determined by $2/\max q$; stronger gradients enable to encode higher spatial frequencies. The displacement field of view $\max |\mathbf{R}|$ is determined by radial sampling density $2/\Delta q$. The choice of δ and $\max q$ implies a trade-off between resolution, achieved maximizing $\max q$, and accuracy, achieved minimizing δ ; the scale of the compartment to probe sets the minimum value for $\max q$ (16).

It is instructive to consider two limiting cases. $P(\mathbf{R}, \tau \rightarrow 0)$ is an infinitely narrow Gaussian isotropic propagator (Eq. [22]). Considering restricted diffusion in an isolated pore with nonrelaxing and impermeable barriers, from Eq. [26] we have

$$P(\mathbf{R}, \tau \rightarrow \infty) = \int \chi(\mathbf{r} + \mathbf{R})\chi(\mathbf{r})d\mathbf{r}, \quad [131]$$

since in the Markovian regime $\rho(\mathbf{r}) = \chi(\mathbf{r})$; we note that this is the autocorrelation function of molecular density (9, 16, 21, 81). By virtue of the Wiener-Khinchin theorem it follows that

$$P(\mathbf{R}, \tau \rightarrow \infty) = \sum_{\text{pores}} \int \chi(\mathbf{r} + \mathbf{R})\chi(\mathbf{r})d\mathbf{r} = \mathfrak{F}^{-1} \left(\sum_{\text{pores}} |\mathfrak{F}[\chi(\mathbf{r})]|^2 \right), \quad [132]$$

which enables direct inference of the average structure function from the EAP (16, 21, 81). In biological tissues the applicability of this formula is limited by surface relaxation, finite permeability, and high pore connectivity; for example, Sukstanskii et al. have

shown that the EAP measured from a regular array of permeable membranes exhibits deceiving multicompartmental features (22, 61).

As a consequence of the properties of the Fourier transform, the diffusion-weighted signal corresponding to a pseudoperiodic array of pores exhibits multiple peaks: with an optical analogy, this phenomenon is termed *diffusion diffraction* (83). Pictorially, one can think of this phenomenon as of molecules being reflected from the barriers, thus having a higher probability of returning to their initial position, therefore causing signal not to decay monotonically as a function of q (61). These diffraction peaks enable to extract microstructural information on pseudoperiodic samples, a technique known as *diffusion spectroscopy*. In biological tissues these peaks are generally not observed, due to microstructural heterogeneity, and to the permeability and relaxivity of barriers (61).

Figure 15 shows some examples of the relationship between signal decay $s(q, \tau)$ and displacement probability $P(X, \tau)$ for one dimension.

Notwithstanding the fact that in biological tissues diffraction peaks are not visible and that the relationship between microstructure and the EAP is weak, it is possible to extract “apparent” microstructural information. For example, one may generate maps of the probability of zero displacement $P(0, \tau)$, and of displacement at half-height $2P(X_{1/2}, \tau) = P(0, \tau)$. The former can be interpreted as an indicator of restriction, the latter as an inverse indicator of restriction. Known as *displacement imaging*, this technique has been shown to be highly sensitive to pathological changes in myelination, demyelinated areas being characterized by smaller $P(0, \tau)$ and larger $X_{1/2}$, due to loss of highly impermeable myelin sheaths and axonal damage (28, 84).

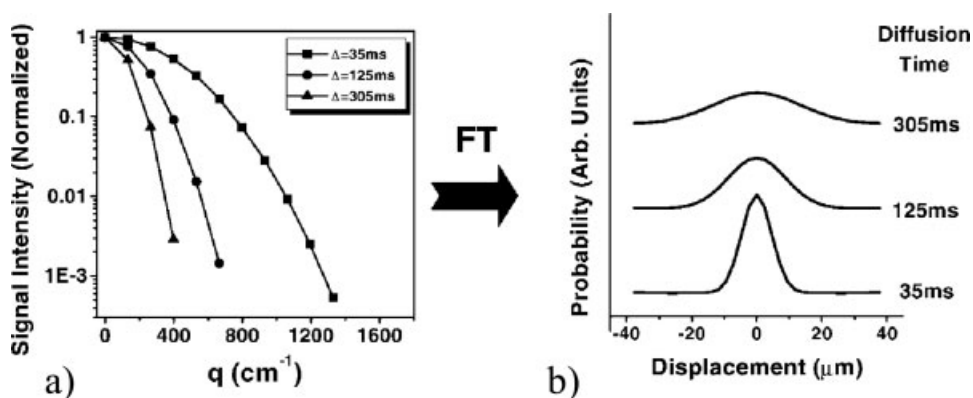


Figure 15 Signal decay $s(q, \tau)$ (a), and corresponding one-dimensional propagator $P(X, \tau)$ (b). (Reproduced from (84) with permission from John Wiley & Sons.) The wider the displacement PDF, the steeper signal decays as a function of q .

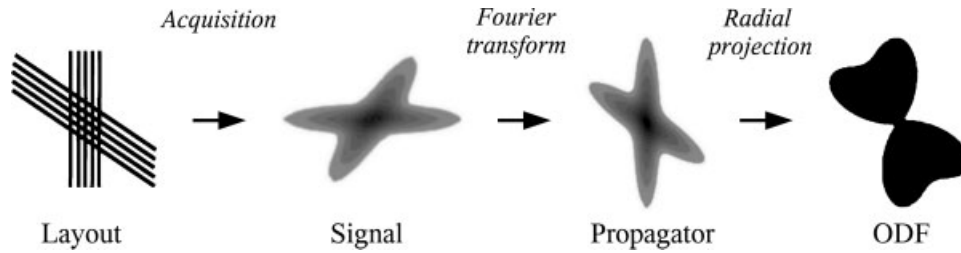


Figure 16 From fibre layout to ODF. The Fourier transform enables to recover the propagator; the displacement isoprobability maxima coincide with fibre orientation. The radial projection provides a value which is a function of angle only.

Recalling from the fourth section that, as opposed to diffusivity, displacement probability is maximum along the directions of fiber orientation, as depicted in Fig. 16 one may reconstruct the ODF by radial projection of the EAP for suitably large values of τ

$$\psi(\mathbf{u}) = k \int_0^{\max|\mathbf{R}|} P(\rho\mathbf{u}, \tau) f(\rho) d\rho, \quad [133]$$

where \mathbf{u} is a unit vector, k is a normalization coefficient, and $f(\rho)$ is a weighting function emphasizing long displacements, often chosen to be $f(\rho) = \rho^2$ (34).

Equation [133] discards the radial information contained in the propagator. In fact, since displacement isoprobability is maximum along the directions of fiber orientation for a range of values of ρ , one need not integrate over ρ and, for suitably chosen values of ρ , the ODF could be approximated with

$$\psi(\mathbf{u}) = kP(\rho\mathbf{u}, \tau), \quad [134]$$

which corresponds to sampling at a single q -value, $q' = 1/\rho$ (85, 86). However, the Fourier transform cannot be calculated with a single q -value. In 2003, Tuch et al. showed that the *Funk–Radon transform* (FRT), which is a generalization of the Radon transform to spherical coordinates, can be used to approximate $\psi(\mathbf{u})$ from measurements taken on a sphere corresponding to a single q -value. The resulting technique, known as *q-ball imaging* (QBI), provides a drastic reduction in acquisition time when compared to sampling on a Cartesian lattice, making in vivo applications possible (85, 86). Due to its high relevance to in vivo brain imaging, we shall present a complete derivation of the relationship between the FRT and radial projection of the propagator.

The FRT, subsequently written as $S[\]$, is a transform from the sphere to the sphere, assigning to a point on the unit sphere the path integral over the corresponding equator (87)

$$S[f(\mathbf{u})] = \int_{\mathbf{v} \perp \mathbf{u}} f(\mathbf{v}) d\mathbf{v} = \int_S f(\mathbf{v}) \delta(\mathbf{v} \cdot \mathbf{u}) d\mathbf{v}. \quad [135]$$

Adapting from (85), for convenience we shall use cylindrical coordinates for $s(q_r, q_\theta, q_z)$ and $P(r, \theta, z)$ (τ is omitted for brevity); without loss of generality, we shall take \mathbf{u} to be the z direction. The FRT at a wavevector radius q' on the $z' = 0$ plane can be written as

$$S_{q'}[s] = \int_{-\infty}^{\infty} \int_0^{2\pi} \int_0^{\infty} s(q_r, q_\theta, q_z) \delta(q_z) \times \delta(q_r - q') q_r dq_r dq_\theta dq_z. \quad [136]$$

From the properties of the Delta function, we have

$$S_{q'}[s] = \int_0^{2\pi} \int_0^{\infty} s(q_r, q_\theta, 0) \delta(q_r - q') q_r dq_r dq_\theta. \quad [137]$$

From Parseval's theorem we have

$$\int_{-\infty}^{\infty} f(x) g^*(x) dx = \int_{-\infty}^{\infty} \Im[f] \Im^{-1}[g] dk, \quad [138]$$

which can be extended to cylindrical coordinates.

Let $f = s(q_r, q_\theta, 0)$ and $g = \delta(q_r - q')$, we can write

$$S_{q'}[s] = \int_0^{2\pi} \int_0^{\infty} \Im[s(q_r, q_\theta, 0)] \Im^{-1}[\delta(q_r - q')] r dr d\theta. \quad [139]$$

Since $q' > 0$, we have

$$\Im^{-1}[\delta(q_r - q')] = q' \int_0^{2\pi} e^{2\pi i q' r \cos(q_\theta - \theta)} dq_\theta. \quad [140]$$

Substituting $\alpha = q_\theta - \theta$, we can rewrite this integral as

$$\Im^{-1}[\delta(q_r - q')] = q' \left(\int_{-\theta}^{\theta} e^{2\pi i q' r \cos \alpha} d\alpha + \int_0^{2\pi} e^{2\pi i q' r \cos \alpha} d\alpha - \int_{2\pi - \theta}^{2\pi} e^{2\pi i q' r \cos \alpha} d\alpha \right). \quad [141]$$

Substituting $\beta = \alpha - 2\pi$ in the last right-hand side term, we obtain

$$\mathfrak{F}^{-1}[\delta(q_r - q')] = q' \int_0^{2\pi} e^{2\pi i q' r \cos \alpha} d\alpha. \quad [142]$$

Recalling a definition for the 0th-order Bessel function,

$$J_0(x) = \frac{1}{2\pi} \int_0^{2\pi} e^{ix \cos \theta} d\theta, \quad [143]$$

we come to

$$\mathfrak{F}^{-1}[\delta(q_r - q')] = 2\pi q' J_0(2\pi q' r). \quad [144]$$

Applying the central slice theorem to the Fourier transform of $s(q_r, q_\theta, 0)$ in Eq. [139] gives us that

$$\mathfrak{F}[s(r, \theta, 0)] = \int_{-\infty}^{\infty} P(r, \theta, z) dz. \quad [145]$$

Substituting Eqs. [144] and [145] in Eq. [139], we obtain

$$S_{q'}[s] = 2\pi q' \int_{-\infty}^{\infty} \int_0^{2\pi} \int_0^{\infty} P(r, \theta, z) J_0(2\pi q' r) r dr d\theta dz. \quad [146]$$

If we assume that the mass of J_0 is concentrated at the origin, that is $J_0(x) = \delta(x)$, we come to

$$\begin{aligned} S_{q'}[s] &= 2\pi q' \int_{-\infty}^{\infty} \int_0^{2\pi} \int_0^{\infty} P(r, \theta, z) \delta(2\pi q' r) r dr d\theta dz \\ &= \int_{-\infty}^{\infty} \int_0^{2\pi} \int_0^{\infty} P(r, \theta, z) \delta(r) r dr d\theta dz, \end{aligned} \quad [147]$$

which is the radial projection of $P(r, \theta, z)$ along the z -axis; this assumption introduces error, in the form of blurring of the reconstructed angular pattern.

Therefore, summing over a circle in Fourier space corresponds to the radial projection in displacement space.

According to the Rayleigh definition, the resolution is given by the radial distance of the first zero-crossing of the Bessel function, $\Delta r \approx 0.383/q'$, which is controlled by the radius of the sampling sphere (86).

The QBI approximation of the ODF is given by

$$\Psi(\mathbf{u}) \approx \frac{1}{Z} S[s(\mathbf{q})], \quad [148]$$

with normalization coefficient

$$Z = \int_S S[s(\mathbf{q})] d\mathbf{q}. \quad [149]$$

Analogously to diffusivity patterns, $\psi(\mathbf{u})$ can be represented with a parameterized surface (Eq. [100]). Since peaks corresponding to fiber orientation are superimposed to a large baseline, for visualization purposes a rescaling of the form

$$\psi'(\mathbf{u}) = \frac{\psi(\mathbf{u}) - \min(\psi(\mathbf{u}))}{\max(\psi(\mathbf{u})) - \min(\psi(\mathbf{u}))} \quad [150]$$

is introduced (86).

As shown in Fig. 17, direction-coded color-maps can be obtained from the direction maximizing $\psi(\mathbf{u})$ in each voxel.

QBI reconstruction is computationally very efficient thanks to the fact that the FRT and interpolation can be formulated as multiplication of the signal vector by a precomputed transformation matrix; a detailed presentation of the algorithm can be found in Ref. (86).

IX. SUMMARY

Diffusion can be modeled by means of diffusion coefficients and diffusion tensors if the displacement PDF is assumed to be Gaussian, or, more generally, by means of the formalism of propagators. The statistical properties of self-diffusion of water molecules in the brain parenchyma are to a large extent determined by cell membranes and myelin sheaths. While the relationship with microstructure can be very complex, some simplified limits were presented. Their validity is limited due to membrane permeability and relaxation, and due to physiological activity.

The diffusion-weighted signal can be modeled in terms of diffusion of magnetization (by means of the Bloch–Torrey equation) or in terms of diffusion of spin-bearing particles (by means of the cumulant expansion). For the case of Gaussian diffusion, both lead to the Stejskal–Tanner equation. Cumulant expansion provides a straightforward framework to account for deviation from Gaussian behavior by introducing higher-order cumulants.

Rank-2 DTI builds on the assumption of monomodal Gaussian diffusion. By decomposing diagonalized tensors in isotropic and deviatoric components, rotation-invariant measures of diffusion anisotropy can be obtained. Assuming that the direction of maximum diffusivity is tangent to the path of coherently-oriented axonal bundles enables to visualize their orientation through direction-coded color maps. In regions where IVOH is present, rank-2 tensors take an oblate shape, preventing from resolving orientation and leading to underestimation of anisotropy.

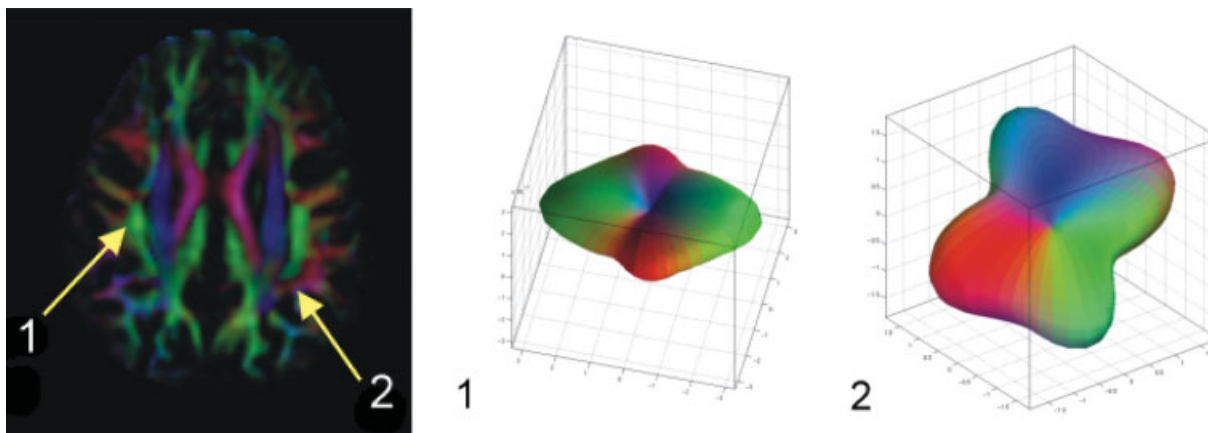


Figure 17 An example of Q -ball colour-map and ODF. Although the colour-map bears a major similarity with those obtained with rank-2 DTI, QBI reveals crossing of commissural (red) and association (green) fibres (1), and of association (green) and projection (blue) fibres (2). From data acquired on a healthy volunteer at 1.5T at Helimed diagnostic imaging sp. z o.o. (Katowice, Poland). [Color figure can be viewed in the online issue, which is available at www.interscience.wiley.com.]

It is found that the decay of the diffusion-weighted signal is well fit by a biexponential model. Although tempting, the interpretation of the two components in terms of intra- and extracellular compartments is generally not possible. Evidences of this are unphysiological predictions of the volume fraction, and the fact that compartmentalization is not a prerequisite for biexponential decay.

When multiple heterogeneously oriented fibers are considered, it is found that while the maxima of displacement isoprobability correspond to fiber orientation, diffusivity maxima do not. On the basis of the assumption of independent addition of signal, a Gaussian mixture model can be set up. While revealing fiber orientation and volume fraction, such a model has the major limitations of requiring to assume a priori a discrete number of orientations, and of leading to unstable fitting for more than two orientations.

The concept of diffusion tensor can be generalized to arbitrary rank, either by preserving the assumption of Gaussianity and using a single tensor to represent the angular diffusivity pattern, or by expanding Fick's laws in series of tensors of increasing rank.

The variance-based definition of anisotropy introduced for the rank-2 tensor can be generalized to any function defined on the unit sphere; it is also possible to consider orientation as the random variable and normalized diffusivity as its distribution. This provides two measures of anisotropy applicable to higher-order tensors.

Decomposition of angular diffusivity patterns in terms of real combinations of the spherical harmonics enables to separate isotropic, monomodal, and multimodal components. It enables to detect the presence of multiple fibers by means of indexes of fiber multiplicity (FMI) or statistical tests. Reconstruction of the ODF by means of deconvolution of the diffusion-weighted signal can be written as a series of matrix operations computing the SHD coefficients of the ODF from those of the signal.

The Fourier relationship between signal and displacement at the basis of cumulant expansion can be naturally extended to three dimensions. This enables to reconstruct the EAP without a priori assumptions. As long as one assumes that no net flux occurs, no information is lost by considering the signal magnitude. In biological tissues, diffraction peaks are normally not observed and the relationship between the EAP and microstructure is made weak by membrane permeability and relaxivity. Nevertheless, measurement of the zero-displacement probability and of displacement at half-height can provide information on "apparent" microstructure.

The ODF can be reconstructed by means of radial projection of the propagator, or, more efficiently, by means the FRT, which can be applied to measurements taken on a sphere rather than on a Cartesian lattice. It can be shown that the FRT, which can be written in matrix form, is equivalent to the radial projection of the propagator, to the extent to which the mass of a zero-order Bessel function is assumed to be concentrated at the origin.

REFERENCES

1. Stejskal EO, Tanner JE. 1965. Spin diffusion measurements: spin echoes in the presence of a time-dependent field gradient. *J Chem Phys* 42:288–229.
2. Stejskal EO. 1965. Use of spin echoes in a pulsed magnetic-field gradient to study anisotropic, restricted diffusion and flow. *J Chem Phys* 43:3597–3603.
3. Le Bihan D, Breton E, Lallemand D. 1986. MR imaging of intravoxel incoherent motions: application to diffusion and perfusion in neurologic disorders. *Radiology* 161:401–407.
4. Moseley ME, Cohen Y, Kucharczyk J, et al. 1990. Diffusion-weighted MR imaging of anisotropic water diffusion in cat central nervous system. *Radiology* 176:439–445.
5. Masutani Y, Aoki S, Abe O, Hayashi N, Otomo K. 2003. MR diffusion tensor imaging: recent advance and new techniques for diffusion tensor visualization. *Eur J Radiol* 46:53–66.
6. Price W. 1997. Pulsed-field gradient nuclear magnetic resonance as a tool for studying translational diffusion: Part 1. Basic theory. *Concepts Magn Reson* 9:299–336.
7. Price W. 1997. Pulsed-field gradient nuclear magnetic resonance as a tool for studying translational diffusion: Part II. Experimental aspects. *Concepts Magn Reson* 10:197–237.
8. Lenk R. 1977. *Brownian Motion and Spin Relaxation*. Amsterdam: Elsevier.
9. Green MS. 1954. Markov random process and the statistical mechanics of time dependent phenomena. Irreversible processes in fluids. *J Chem Phys* 22:398–412.
10. Landau LD, Lifschitz EM, eds. 1999. *Statistical Physics*. New York: Butterworth-Heinemann.
11. Crank J. 1975. *The Mathematics of Diffusion*. London: Oxford University Press.
12. Fick A. 1855. On liquid diffusion. *Philos Mag* 10:30–39.
13. Onsager L. 1936. Electric moments of molecules in liquids. *J Am Chem Soc* 58:1486–1493.
14. Basser PJ. 1995. Inferring microstructural features and the physiological state of tissues from diffusion-weighted images. *NMR Biomed* 8:333–344.
15. Karger J, Heink W. 1983. The propagator representation of molecular transport in microporous crystallites. *J Magn Reson* 51:1–7.
16. Callaghan PT. 1993. *Principles of Nuclear Magnetic Resonance Microscopy*. London: Oxford University Press.
17. Risken H. 1989. *The Fokker–Planck Equation: Methods of Solutions and Applications*. New York, Springer.
18. Einstein A. 1956. *Investigations on the Theory of Brownian Movement*. New York: Dover.
19. Le Bihan D. 1995. Molecular diffusion, tissue microdynamics and microstructure. *NMR Biomed* 8:375–386.
20. Ford JC, Hackney DB, Lavi E, Phillips M, Patel U. 1998. Dependence of apparent diffusion coefficients on axonal spacing, membrane permeability, and diffusion time in spinal cord white matter. *J Magn Reson Imaging* 8:775–782.
21. Cory DG, Garroway AN. 1990. Measurement of translational displacement probabilities by NMR: an indicator of compartmentation. *Magn Reson Med* 14:435–444.
22. Sukstanskii AL, Yablonskiy DA, Ackerman JH. 2004. Effects of permeable boundaries on the diffusion-attenuated MR signal: insight from a one-dimensional model. *J Magn Reson* 170:56–66.
23. Beaulieu C. 2002. The basis of anisotropic water diffusion in the nervous system—a technical review. *NMR Biomed* 15:435–455.
24. Beaulieu C, Allen PS. 1994. Determinants of anisotropic water diffusion in nerves. *Magn Reson Med* 31:394–400.
25. Torrey HC. 1956. Bloch equations with diffusion terms. *Phys Rev* 104:563–565.
26. Wang LZ, Caprihan Z, Fukushima E. 1995. The narrow-pulse criterion for pulsed-gradient spin-echo diffusion measurements. *J Magn Reson A* 117:209–219.
27. Mitra PP, Halperin BI. 1995. The narrow-pulse criterion for pulsed-gradient spin-echo diffusion measurements. *J Magn Reson A* 113:94–101.
28. Assaf Y, Ben-Bashat D, Chapman J, Peled S, Biton IE, Kafri M, Segev Y, Hendler T, Korczyn AD, Graif M, Cohen Y. 2002. High b-value q-space analyzed diffusion-weighted MRI: application to multiple sclerosis. *Magn Reson Med* 47:115–122.
29. Le Bihan D. 1991. Molecular diffusion nuclear magnetic resonance imaging. *Magn Reson Q* 7:1–30.
30. Mattiello J, Basser PJ, LeBihan D. 1994. Analytical expressions for the b matrix in NMR diffusion imaging and spectroscopy. *J Magn Res A* 108:131–141.
31. Abramowitz M, Stegun IA. 1972. *Handbook of Mathematical Functions with Formulas, Graphs, and Mathematical Tables*. New York: Dover. p. 928.
32. Frohlich AF, Ostergaard L, Kiselev VG. 2005. Effect of impermeable interfaces on apparent diffusion coefficient in heterogeneous media. *Appl Magn Reson* 28:123–137.
33. Frohlich AF, Ostergaard L, Kiselev VG. 2006. Effect of impermeable boundaries on diffusion-attenuated MR signal. *J Magn Reson* 179:223–233.
34. Wedeen VJ, Hagmann P, Tseng WY, Reese TG, Weisskoff RM. 2005. Mapping complex tissue architecture with diffusion spectrum magnetic resonance imaging. *Magn Reson Med* 54:1377–1386.
35. Jensen JH, Helpert JA, Ramani A, Lu H, Kaczynski K. 2005. Diffusional kurtosis imaging: the quantification of non-Gaussian water diffusion by means of magnetic resonance imaging. *Magn Reson Med* 53:1432–1440.
36. Minati L, Bruzzone MG, Grisoli G, Maccagnano C, Rampoldi S, Banasik T, Mandelli ML, Farina L. 2006. Preliminary findings with diffusional

- kurtosis imaging (DKI) of brain tumours. In: 23rd Meeting of the European Society for Magnetic Resonance in Medicine and Biology, Warsaw. EPOS #574.
37. Joanes DN, Gill CA. 1998. Comparing measures of sample skewness and kurtosis. *J Roy Stat Soc D* 47: 183–189.
 38. Lu H, Jensen JH, Ramani A, Helpert JA. 2006. Three-dimensional characterization of non-Gaussian water diffusion in humans using diffusion kurtosis imaging. *NMR Biomed* 19:236–247.
 39. Le Bihan D, Turner R, Douek P. 1993. Is water diffusion restricted in human brain white matter? An echo planar NMR imaging study. *NeuroReport* 4: 887–890.
 40. Pilatus U, Shim H, Artemov D, Davis D, van Zijl PC, Glickson JD. 1997. Intracellular volume and apparent diffusion constants of perfused cancer cell cultures, as measured by NMR. *Magn Reson Med* 37:825–832.
 41. Reese TG, Heid O, Weissko RM, Wedeen VJ. 2003. Reduction of eddy-current-induced distortion in diffusion MRI using a twice-refocused spin echo. *Magn Reson Med* 49:177–182.
 42. Jones DK, Horsfield MA, Simmons A. 1999. Optimal strategies for measuring diffusion in anisotropic systems by magnetic resonance imaging. *Magn Reson Med* 42:515–525.
 43. Basser PJ, Mattiello J, LeBihan D. 1994. Estimation of the effective self-diffusion tensor from the NMR spin echo. *J Magn Reson B* 103:247–254.
 44. Il'yasov KA, Barta G, Kreher BW, Bellemann ME, Hennig J. 2005. Importance of exact b-tensor calculation for quantitative diffusion tensor imaging and tracking of neuronal fiber bundles. *Appl Magn Res* 29:107–122.
 45. Hasan KM, Basser PJ, Parker DL, Alexander AL. 2001. Analytical computation of the eigenvalues and eigenvectors in DT-MRI. *J Magn Reson* 152:41–47.
 46. Abdi H. 2007. Singular value decomposition (SVD) and generalized singular value decomposition (GSVD). In: Salkind NJ, ed. *Encyclopedia of Measurement and Statistics*. Thousand Oaks CA: Sage.
 47. Basser PJ, Pajevic S, Pierpaoli C, Duda J, Aldroubi A. 2000. In vivo fiber tractography using DT-MRI data. *Magn Reson Med* 44:625–632.
 48. Basser PJ, Pierpaoli C. 1996. Microstructural and physiological features of tissues elucidated by quantitative-diffusion-tensor MRI. *J Magn Reson B* 111: 209–219.
 49. Hasan KM, Alexander AL, Narayana PA. 2004. Does fractional anisotropy have better noise immunity characteristics than relative anisotropy in diffusion tensor MRI? An analytical approach. *Magn Reson Med* 51: 413–417.
 50. Minati L, Banasik T, Brzezinski J, Mandelli ML, Bizzi A, Bruzzone MG, Jasinski A. 2007. Elevating tensor rank increases anisotropy in brain areas associated with orientational heterogeneity (IVOH): a generalised DTI (GDTI) study. *NMR Biomed* (in press).
 51. Pajevic S, Pierpaoli C. 1999. Color schemes to represent the orientation of anisotropic tissues from diffusion tensor data: application to white matter fiber tract mapping in the human brain. *Magn Reson Med* 42:526–540.
 52. Westin CF, Maier SE, Mamata H, Nabavi A, Jolesz FA, Kikinis R. 2002. Processing and visualization for diffusion tensor MRI. *Med Image Anal* 6:93–108.
 53. Tuch DS, Reese TG, Wiegell MR, Makris N, Belliveau JW, Wedeen VJ. 2002. High angular resolution diffusion imaging reveals intravoxel white matter fiber heterogeneity. *Magn Reson Med* 48:577–582.
 54. Wedeen VJ, Reese TG, Napadow VJ, Gilbert RJ. 2001. Demonstration of primary and secondary muscle fiber architecture of the bovine tongue by diffusion tensor magnetic resonance imaging. *Biophys J* 80:1024–1028.
 55. Pierpaoli C, Barnett A, Pajevic S, Chen R, Penix L, Virta A, Basser P. 2001. Water diffusion changes in Wallerian degeneration and their dependence on white matter architecture. *NeuroImage* 13:1174–1185.
 56. Niendorf T, Dijkhuizen RM, Norris DG, van Lookeren Campagne M, Nicolay K. 1996. Biexponential diffusion attenuation in various states of brain tissue: implications for diffusion-weighted imaging. *Magn Reson Med* 36:847–857.
 57. Clark CA, Le Bihan D. 2000. Water diffusion compartmentation and anisotropy at high b values in the human brain. *Magn Reson Med* 44:852–859.
 58. Mulkern RV, Zengingonul HP, Robertson RL, Bogner P, Zou KH, Gudbjartsson H, et al. 2000. Multi-component apparent diffusion coefficients in human brain: relationship to spin-lattice relaxation. *Magn Reson Med* 44:292–300.
 59. Sukstanskii AL, Yablonskiy DA. 2003. Effects of barrier-induced nuclear spin magnetization inhomogeneities on diffusion-attenuated MR signal. *Magn Reson Med* 50:735–742.
 60. Sukstanskii AL, Ackerman JJH, Yablonskiy DA. 2002. Effects of restricted diffusion on MR signal formation. *J Magn Reson* 157:95–105.
 61. Cohen Y, Assaf Y. 2002. High b-value q-space analyzed diffusion-weighted MRS and MRI in neuronal tissues—a technical review. *NMR Biomed* 15:516–542.
 62. Schwarcz A, Bogner P, Meric P, Correze J, Berente Z, Pal J, Gallyas F, Doczi T, Gillet B, Beloeil J. 2004. The existence of biexponential signal decay in magnetic resonance diffusion-weighted imaging appears to be independent of compartmentalization. *Magn Reson Med* 51:278–285.
 63. Wiegell M, Larsson HB, Wedeen J. 2000. Fiber crossing in human brain depicted with diffusion tensor MR imaging. *Radiology* 217:897–903.
 64. Ozarslan E, Shepherd TM, Vemuri BC, Blackband SJ, Mareci TH. 2006. Resolution of complex tissue microarchitecture using the diffusion orientation transform (DOT). *Neuroimage* 31:1086–1103.
 65. Hosey T, Williams G, Ansoorge R. 2005. Inference of multiple fiber orientations in high angular resolution diffusion imaging. *Magn Reson Med* 54:1480–1489.

66. Kreher BW, Schneider JF, Mader I, Martin E, Hennig J, Il'yasov KA. 2005. Multitensor approach for analysis and tracking of complex fiber configurations. *Magn Reson Med* 54:1216–1225.
67. Assaf Y, Freidlin RZ, Rohde GK, Basser PJ. 2004. New modeling and experimental framework to characterize hindered and restricted water diffusion in brain white matter. *Magn Reson Med* 52:965–978.
68. Stanisz GJ, Szafer A, Wright GA, Henkelman RM. 1997. An analytical model of restricted diffusion in bovine optic nerve. *Magn Reson Med* 37:303–311.
69. Schouten JA. 1989. *Tensor Analysis for Physicists*. New York: Dover.
70. Carroll JD, Chang J. 1970. Analysis of individual differences in multidimensional scaling via an N-way generalization of 'Eckart-Young' decomposition. *Psychometrika* 35:283–319.
71. Tucker LR. 1966. Some mathematical notes on three-mode factor analysis. *Psychometrika* 31:279–311.
72. Ozarslan E, Mareci TH. 2003. Generalized diffusion tensor imaging and analytical relationships between diffusion tensor imaging and high angular resolution diffusion imaging. *Magn Reson Med* 50:955–965.
73. Liu C, Bammer R, Acar B, Moseley ME. 2004. Characterizing non-Gaussian diffusion by using generalized diffusion tensors. *Magn Reson Med* 51:924–937.
74. Ozarslan E, Vemuri BC, Mareci T. 2005. Generalized scalar measures for diffusion MRI using trace, variance, and entropy. *Magn Reson Med* 53:866–876.
75. MacRobert TM, Sneddon IN. 1967. *Spherical Harmonics: An Elementary Treatise on Harmonic Functions, with Applications*. Oxford: Pergamon Press.
76. Wigner EP. 2002. *Gruppentheorie und ihre Anwendungen auf die Quantenmechanik der Atomspektren*. Braunschweig: Vieweg Verlag, 1931.
77. Frank LR. Characterization of anisotropy in high angular resolution diffusion-weighted MRI. *Magn Reson Med* 47:1083–1099.
78. Alexander DC, Barker GJ, Arridge SR. 2002. Detection and modeling of non-Gaussian apparent diffusion coefficient profiles in human brain data. *Magn Reson Med* 48:331–340.
79. Zhan W, Gu H, Xu S, Silbersweig DA, Stern E, Yang Y. 2003. Circular spectrum mapping for intravoxel fiber structures based on high angular resolution apparent diffusion coefficients. *Magn Reson Med* 49:1077–1088.
80. Tournier JD, Calamante F, Gadian FD, Connelly A. 2004. Direct estimation of the fiber orientation density function from diffusion-weighted MRI data using spherical deconvolution. *NeuroImage* 23:1176–1185.
81. Callaghan PT, MacGowan D, Packer KJ, Zelaya FO. 1990. High resolution q-space imaging in porous structures. *J Magn Reson* 90:177–182.
82. Pickalov V, Basser PJ. 2006. 3D tomographic reconstruction of the average propagator from MRI data. *Proc IEEE ISBI*. pp. 710–713.
83. Callaghan PT, Coy A, MacGowan D, Packer KJ, Zelaya FO. 1991. Diffraction-like effects in NMR diffusion studies of fluids in porous solids. *Nature* 351:467–469.
84. Assaf Y, Cohen Y. 2000. Assignment of the water slow diffusing component in CNS using q-space diffusion MRS: implications to fiber tract imaging. *Magn Reson Med* 43:191–199.
85. Tuch DS, Reese TG, Wiegell MR, Wedeen VJ. 2003. Diffusion MRI of complex neural architecture. *Neuron* 40:885–895.
86. Tuch DS. 2004. Q-ball imaging. *Magn Reson Med* 52:1358–1372.
87. Funk P. 1916. Über eine geometrische Anwendung der Abelschen Integralgleichung. *Math Ann* 77:129–135.

BIOGRAPHIES



Ludovico Minati received his B.Sc. and M.Sc. from The Open University, Milton Keynes, UK, in 2004 and 2006 respectively. After 4 years in the field of robotics, design of integrated circuits, vision systems, and monitoring devices, he joined the “Carlo Besta” National Neurological Institute, Milan, Italy, in 2005, where he has since been active in the field of advanced MR imaging. His topics of active research have included imaging in Parkinson’s disease and ageing, functional MRI in malformations of cortical development, quantitative ^1H spectroscopy, and novel forms of clinically-applicable diffusion imaging, including generalized diffusion-tensor imaging, and the application of biexponential and kurtosis models. He is currently studying towards a M.Sc. in cognitive neuroscience, and active in the field of combination of functional MRI and event-related potentials (ERP).



Wladyslaw P. Węglarz received his M.Sc. in Physics at the Jagiellonian University in Kraków, Poland, in 1988, and his Ph.D. from the Institute of Nuclear Physics (INP), Polish Academy of Sciences, Kraków, in 1994. Until 1999 he has been postdoctoral fellow and visiting scientist at the University of Waterloo, Canada, conducting research on water interfaces in hydrated biopolymers, characterization of synthetic polymers and porous materials, and computer simulations of macromolecular structure and dynamics of hydrated biomolecules. Since 1995 he has been with the MRI laboratory at the INP, conducting research on MR methods for diffusion imaging in a model of spinal cord injury. From 2005 to 2007 he has been at the Unilever Food and Health Research Institute, Vlaardingen, The Netherlands with a Marie Curie fellowship, conducting research on water migration and mobility in multicomponent food model systems. He currently leads projects on applications of MRI and MRS in biomedicine and pharmacology at the INP, Polish Academy of Sciences, Kraków.